

AD \_\_\_\_\_

AWARD NUMBER: W81XWH-08-1-0331

TITLE: System Design, Algorithm Development, and Verification for Optoacoustic Molecular Imaging of Protease Expression in Breast Cancer

PRINCIPAL INVESTIGATOR: Dimple Modgil

CONTRACTING ORGANIZATION: University of Chicago  
Chicago, IL 60637

REPORT DATE: May 2009

TYPE OF REPORT: Annual

PREPARED FOR: U.S. Army Medical Research and Materiel Command  
Fort Detrick, Maryland 21702-5012

DISTRIBUTION STATEMENT: Approved for Public Release;  
Distribution Unlimited

The views, opinions and/or findings contained in this report are those of the author(s) and should not be construed as an official Department of the Army position, policy or decision unless so designated by other documentation.

REPORT DOCUMENTATION PAGE				Form Approved OMB No. 0704-0188	
Public reporting burden for this collection of information is estimated to average 1 hour per response, including the time for reviewing instructions, searching existing data sources, gathering and maintaining the data needed, and completing and reviewing this collection of information. Send comments regarding this burden estimate or any other aspect of this collection of information, including suggestions for reducing this burden to Department of Defense, Washington Headquarters Services, Directorate for Information Operations and Reports (0704-0188), 1215 Jefferson Davis Highway, Suite 1204, Arlington, VA 22202-4302. Respondents should be aware that notwithstanding any other provision of law, no person shall be subject to any penalty for failing to comply with a collection of information if it does not display a currently valid OMB control number. <b>PLEASE DO NOT RETURN YOUR FORM TO THE ABOVE ADDRESS.</b>					
1. REPORT DATE 1 May 2009		2. REPORT TYPE Annual		3. DATES COVERED 1 May 2008 – 30 Apr 2009	
4. TITLE AND SUBTITLE  System Design, Algorithm Development, and Verification for Optoacoustic Molecular Imaging of Protease Expression in Breast Cancer				5a. CONTRACT NUMBER	
				5b. GRANT NUMBER W81XWH-08-1-0331	
				5c. PROGRAM ELEMENT NUMBER	
6. AUTHOR(S)  Dimple Modgil  E-Mail: dimple@uchicago.edu				5d. PROJECT NUMBER	
				5e. TASK NUMBER	
				5f. WORK UNIT NUMBER	
7. PERFORMING ORGANIZATION NAME(S) AND ADDRESS(ES)  University of Chicago Chicago, IL 60637				8. PERFORMING ORGANIZATION REPORT NUMBER	
9. SPONSORING / MONITORING AGENCY NAME(S) AND ADDRESS(ES) U.S. Army Medical Research and Materiel Command Fort Detrick, Maryland 21702-5012				10. SPONSOR/MONITOR'S ACRONYM(S)	
				11. SPONSOR/MONITOR'S REPORT NUMBER(S)	
12. DISTRIBUTION / AVAILABILITY STATEMENT Approved for Public Release; Distribution Unlimited					
13. SUPPLEMENTARY NOTES					
14. ABSTRACT Optoacoustic tomography (OAT) is an emerging, hybrid technique that is non-invasive and uses non-ionizing radiation. No one has yet developed a molecular probe for early detection of proteases in breast cancer using OAT. Our group is developing a molecular probe and an optoacoustic imaging system to address this. During the first year of this project, we have implemented the code that simulates the ideal optoacoustic system. We have compared existing 2D algorithms in OAT with respect to contrast, resolution, noise and signal detectability. We also explored the effect of variable speed of sound and ultrasonic attenuation on image quality. We derived new techniques to address these physical effects that could cause image distortion and blurring.					
15. SUBJECT TERMS optoacoustic, photoacoustic, molecular imaging, proteases					
16. SECURITY CLASSIFICATION OF:			17. LIMITATION OF ABSTRACT	18. NUMBER OF PAGES	19a. NAME OF RESPONSIBLE PERSON
a. REPORT U	b. ABSTRACT U	c. THIS PAGE U			USAMRMC
			UU		19b. TELEPHONE NUMBER (include area code)

## Table of Contents

	<u>Page</u>
Introduction.....	2
Body.....	3
Key Research Accomplishments.....	5
Reportable Outcomes.....	6
Conclusion.....	7
References.....	8
Appendices.....	9

## **Introduction**

Optoacoustic tomography (OAT) is an emerging, hybrid modality that offers high contrast of optical imaging along with high resolution of ultrasound imaging [1]. While several groups have looked at the application of OAT in detection of breast cancer [1] and optoacoustic molecular imaging (OMI) [3] no one has yet looked using OMI for breast cancer using proteases as target. Elevated levels of protease are found in several cancers including breast cancer [2]. This proposal will aid in the design and development of an optoacoustic molecular imaging system specifically targeted to detect elevated levels of protease. We are specifically implementing software that will simulate the following: ideal optoacoustic signal, effect of finite transducer width and temporal response, effect of non-uniform illumination, effect of variable speed of sound, and effect of ultrasonic attenuation. In addition, we will compare the various image reconstruction algorithms, validate the simulations using experimental data and refine the optoacoustic device design.

This technique has the potential to detect breast cancer earlier than mammography, especially in young women with radiographically dense breasts. It also has the potential to allow for molecular characterization of tumors in women of all ages. This technique has also the added advantage of being non-invasive and involves no ionizing radiation. It is also relatively inexpensive with costs comparable to that of ultrasound

This report summarized the progress made on this pre-doctoral traineeship project for breast cancer by the recipient during the past year.

## Body

### Training:

The program requires 22 courses over all. However, the applicant needs to take only 15 courses since she has a Masters degree in Physics and had previous teaching experience. The applicant has taken 14 of the required 15 courses. The courses taken in the past year include cancer biology.

### Research Accomplishments

The main goals of this project are:

- (1) developing and implementing simulations of optoacoustic physics and signal detection with a handheld optoacoustic probe, with the aim of performing optoacoustic molecular imaging.
- (2) validating the simulation software by comparing it with actual optoacoustic signal generation and detection in the laboratory.
- (3) comparing image-reconstruction software for optoacoustic image with a handheld probe.
- (4) using these tools to refine the design of the optoacoustic image device.

We performed the following research during the past year:

#### 1. Development of ideal optoacoustic signal software

We have developed the ideal optoacoustic signal software for the specific 2D geometry that we are considering. In this geometry the transducer is scanned along a line and the inherently 3D problem is reduced to 2D because of transducer's directivity. We have also included the finite length of the stimulating pulse and the finite temporal response of the transducer in to our simulation software. Both these effects are assumed to be ideal delta functions in most reconstruction algorithms.

#### 2. Studying the effect of variable speed of sound and ultrasonic attenuation

There are several physical factors that impact image quality in OAT. These include limited data, noise, non-uniform illumination, variable speed of sound and ultrasonic attenuation. There are several investigators looking at the problems of limited data and non-uniform illumination. We investigated two of these factors: variable speed of sound and ultrasonic attenuation.

The majority of the image reconstruction algorithms in optoacoustic tomography (OAT) so far have assumed a uniform, non-dispersive acoustic medium. The effect of frequency-dependent attenuation on acoustic waves can be significant since OAT uses broadband detection. Reconstructed images may exhibit distortion and artifacts if these effects are not taken into account. Previous work on dispersive acoustic media done by our group [4] focused on incorporating the frequency dependent attenuation effects into the OAT model. We explored this effect further and studied the conditioning of the resulting inverse problem. We have derived an inversion formula for the optical absorption function in the presence of attenuation using singular-value decomposition (SVD). This expression relates the measured, attenuated pressure via an integral operator to the optical absorption coefficient of the medium [10]. We also derived another expression for attenuation correction when a source is placed in a medium with different attenuation from that of the source. This is a common scenario in practice where a tumor may have a different attenuation coefficient from that of the surrounding healthy tissue.

Speed of sound can vary in the breast tissue by as much as 10%. The variable speed of sound affects the travel times of the sound waves that reach the transducer. Incorrectly computed travel-times can have an effect on image quality and accuracy. Previous research in this area has only looked at first-order travel-time perturbations[5,6] and has not incorporated the effects of ray bending. We systematically explored

this effect and developed algorithms for incorporating it into our imaging model. We have derived improvements to the zeroth-order geometrical acoustics (GA) model that incorporates second-order perturbations into travel times of sound waves [11]. For homogeneous speed of sound, the travel-time surfaces of equal times (isochrons) are spheres in 3D and circles in 2D. With variable speed of sound these surfaces are distorted based on the variation in speed. Perceivable differences have been detected in the isochronous surfaces in the inhomogeneous case with speed of sound variation of 10% or more.

### **3. Comparison of optoacoustic image reconstruction algorithms**

There are several algorithms that exist in OAT for the 2D geometry that we are considering. However, these algorithms have not been evaluated for noise and resolution properties. It is important to know which algorithm may be best suited for optoacoustic molecular imaging of our molecular probe. We compared three image-reconstruction algorithms for optoacoustic imaging with a handheld probe. Two of these are based on previously published analytical algorithms that assume fairly idealized data and had already been implemented by us in the past year. The first one is the Fourier-based algorithm [7] that is exact in 3D but not in the 2D geometry that we are considering. The second one is the synthetic aperture algorithm [8] that is approximate but is the most commonly used by researchers in the field. The third algorithm is based on Norton's approach for reflection-mode tomography [9] and has been applied by us to OAT for the first time.

We found that the 2D Fourier-based algorithm offers better resolution and local modulation transfer function (LMTF) in the depth direction while Norton's algorithm offers the best lateral resolution [12]. However, we found that in reconstructions of phantoms the images produced by Norton-based algorithm looked the sharpest and more uniform. The LNEQ data suggests that Norton-based algorithm has the best signal detectability.

We will also implement a new algorithm that we have derived using penalized-likelihood iterative algorithms, which have not previously been applied in the context of OAT but which have the potential to model more of the physical degradations inherent in the modality and thus to lead to higher quality images. These results will be validated in the lab in the coming year when the molecular probe becomes available and the imaging system is ready.

### **Key Research Accomplishments**

1. We have developed software that simulates ideal optoacoustic signal. We have also incorporated the finite transducer and finite laser pulse length effects into this simulation software.
2. We have studied the effect of variable speed of sound and have derived a higher-order geometrical acoustics expression that addresses this effect in image reconstruction.
3. We have derived a new way of incorporating the effect of ultrasonic attenuation in optoacoustic image reconstruction.
4. We have performed a systematic comparison of several algorithms for 2D image reconstruction in terms of resolution, contrast, noise and signal detectability properties. We found that an algorithm that was derived by us based on Norton's approach had the best contrast, resolution and signal detectability properties.

## Conclusions

The recipient of the pre-doctoral training award has one more required course left towards completing the PhD. requirements. She also needs to take a course on molecular biology to expand her knowledge of the life sciences.

During the first year of the award, we focused on implementing the foundation of the simulation software that would aid in the design and development of the optoacoustic molecular imaging system being developed by our group. We also systematically studied two very important factors that impact image quality in OAT: variable speed of sound and ultrasonic attenuation. We derived methods to incorporate these into image reconstruction and developed algorithms that can correct for these physical factors. We also systematically evaluated three image reconstruction algorithms in OAT in a homogeneous, non-dispersive medium in 2D. We found that the new algorithm that was applied by us to OAT based on Norton's approach offered the best contrast, resolution and signal detectability.

Our future research will focus on validation of our simulations, recommendations for the design of the OMI system and its refinement.



## **Reportable Outcomes**

### **Peer Reviewed Journals**

"Implementation and comparison of reconstruction algorithms for 2D optoacoustic tomography using a linear array", D.Modgil and P.J.La Riviere, accepted for publication in the Journal of Biomedical Optics, 2009

### **Conference Proceeding Articles**

1. Dimple Modgil, Mark A. Anastasio, Kun Wang and Patrick J. La Riviere, "Image reconstruction in photoacoustic tomography with variable speed of sound using a higher order geometrical acoustics approximation" (Proceedings Paper) Proceedings Vol. 7177, Photons Plus Ultrasound: Imaging and Sensing 2009, Alexander A. Oraevsky; Lihong V. Wang, Editors, 71771A, February 2009
2. Dimple Modgil, Mark A. Anastasio, Patrick J. La Riviere, "Photoacoustic image reconstruction in an attenuating medium using singular value decomposition" (Proceedings Paper) Proceedings Vol. 7177, Photons Plus Ultrasound: Imaging and Sensing 2009, Alexander A. Oraevsky; Lihong V. Wang, Editors, 71771B, February 2009
3. "Photoacoustic image reconstruction in an attenuating medium using singular-value decomposition", Modgil, Dimple La Riviere, Patrick J. Nuclear Science Symposium C Conference Record, 2008. NSS '08. IEEE Pub. Oct. 2008, pp 4489-4493

### **Honors and Awards**

Biological Sciences Division Travel award, University of Chicago, Spring 2009 for SPIE Photonics West meeting, 2009

## References

- [1] M. Xu and L. V. Wang, "Photoacoustic imaging in biomedicine," *Rev. Sci. Instr.* 77, pp. 041101–1–041101–22, Apr 2006.
- [2] U. Mahmood and R. Weissleder, "Near-infrared optical imaging of proteases in cancer", *Molecular Cancer Therapeutics* , vol. 2, 489-496, May 2003
- [3] R. A. Kruger, W. L. Kiser Jr., G. A. Kruger, and K. D. Miller, "Thermoacoustic optical molecular imaging of small animals, *Molecular Imaging*, vol. 2, pp. 113-123, 2003
- [4] P. J. La Rivière, J. Zhang, and M. A. Anastasio, "Image reconstruction in optoacoustic tomography for dispersive acoustic media," *Optics Letters*, vol. 31, 2006
- [5] Y. Xu and L. V. Wang, "Effects of acoustic heterogeneity in breast thermoacoustic tomography," *IEEE Trans. Ultra., Ferro. and Freq. control.* 50, pp. 1134–1146, Sept 2003.
- [6] J. Zhang and M. A. Anastasio, "Reconstruction of speed-of-sound and electromagnetic absorption distributions in photoacoustic tomography," *Proc. SPIE* 6086, pp. 6086 19–1–19–7, 2006.
- [7] K. P. Kostli and P. C. Beard, "Two-dimensional photoacoustic imaging by use of Fourier-transform image reconstruction and a detector with an anisotropic response," *Applied Optics*, vol. 42, pp. 1899–1908, Apr 2003.
- [8] D. Feng, Y. X. Ku, L. V. Wang, "Microwave-induced thermoacoustic tomography: Reconstruction by synthetic aperture", *Med. Phys.*, 28(12), December 2001
- [9] S. J. Norton, "Reconstruction of a reflectivity field from line integrals over circular paths," *J. Acoust. Soc. Am.* 67, pp. 853–863, Mar 1980.
- [10] D. Modgil, M. A. Anastasio, P. J. La Riviere, "Photoacoustic image reconstruction in an attenuating medium using singular value decomposition" (Proceedings Paper), *SPIE Photonics West* 2009
- [11] D. Modgil, M. A. Anastasio, K. Wang and P. J. La Riviere, "Image reconstruction in photoacoustic tomography with variable speed of sound using a higher order geometrical acoustics approximation" (Proceedings Paper), *SPIE Photonics West* 2009.
- [12] D. Modgil and P. J. La Riviere, "Implementation and comparison of reconstruction algorithms for 2D optoacoustic tomography using a linear array", accepted for publication in the *Journal of Biomedical Optics*, 2009

## Appendices

APPENDIX A: **D.Modgil** and P.J.La Riviere , "Implementation and comparison of reconstruction algorithms for 2D optoacoustic tomography using a linear array", , accepted for publication in the Journal of Biomedical Optics, 2009

APPENDIX B: **Dimple Modgil**, Mark A. Anastasio, Kun Wang and Patrick J. La Riviere, "Image reconstruction in photoacoustic tomography with variable speed of sound using a higher order geometrical acoustics approximation" (Proceedings Paper), SPIE Photonics West 2009

APPENDIX C: **Dimple Modgil**, Mark A. Anastasio, Patrick J. La Riviere, "Photoacoustic image reconstruction in an attenuating medium using singular value decomposition" (Proceedings Paper), SPIE Photonics West 2009

APPENDIX D: **D.Modgil** and P.J.La Riviere, "Photoacoustic image reconstruction in an attenuating medium using singular-value decomposition", J. Nuclear Science Symposium C Conference Record, 2008

# Implementation and comparison of reconstruction algorithms for 2D optoacoustic tomography using a linear array

Dimple Modgil and Patrick J. La Rivière  
Department of Radiology, The University of Chicago

## ABSTRACT

The goal of this paper is to compare and contrast various image reconstruction algorithms for optoacoustic tomography (OAT) assuming a finite linear aperture of the kind that arises when using a linear-array transducer. Because such transducers generally have tall, narrow elements, they are essentially insensitive to out of plane acoustic waves, and the usually 3D OAT problem reduces to a 2D problem. Algorithms developed for the 3D problem may not perform optimally in 2D. We have implemented and evaluated a number of previously described OAT algorithms, including an exact (in 3D) Fourier-based algorithm and a synthetic aperture based algorithm. We have also implemented a 2D algorithm developed by Norton for reflection mode tomography that has not, to the best of our knowledge, been applied to OAT before. Our simulation studies of resolution, contrast, noise properties and signal detectability measures suggest that Norton's approach based algorithm has the best contrast, resolution and signal detectability.

**Keywords:** Optoacoustic tomography, photoacoustic tomography, thermoacoustic tomography, image reconstruction

## 1. INTRODUCTION

Optoacoustic imaging is a hybrid imaging technique that has attracted a lot of attention in recent years [1,2]. It is based on the photoacoustic/optoacoustic effect, which refers to acoustic wave generation upon absorption of pulsed optical energy by a medium. A slight rise in temperature of the medium due to the absorption of the incident electromagnetic wave results in thermoelastic expansion. This thermoelastic expansion and subsequent contraction leads to the generation of acoustic waves. Under the constraints of thermal and stress confinement, this thermal expansion leads to a rise in pressure,  $p(\mathbf{r}, t)$ , that satisfies the three-dimensional inhomogeneous wave equation [3]:

$$\frac{\partial^2 p(\mathbf{r}, t)}{\partial t^2} - c^2 \nabla^2 p(\mathbf{r}, t) = \frac{\beta}{C_p} \frac{\partial}{\partial t} H(\mathbf{r}, t), \quad (1)$$

where  $H(\mathbf{r}, t)$ , the heating function, is the thermal energy deposited by the electromagnetic radiation per unit time per unit volume,  $\beta$  is the isobaric volume expansion coefficient, and  $C_p$  is the specific heat of the medium. The heating function can be expressed as the product of a spatially varying absorbed optical energy in the medium,  $A(\mathbf{r})$ , and a time dependent optical illumination function,  $I(t)$ . The absorbed optical energy in the medium is the product of the optical absorption function and the optical fluence.

Optoacoustic tomography is inherently a three-dimensional inverse problem. The sound waves generated by a 3D distribution of optoacoustic sources are spherical waves radiated into the volume surrounding the sources. These 3D optoacoustic signals can be detected using isotropic ultrasound detectors arrayed on a 2D measurement aperture, and a 3D image can be reconstructed using these signals. However, detection of these signals using a 1D linear array of transducers and reconstruction of a 2D image slice is sometimes more practical and cost-effective especially in a clinical setting. The problem can be reduced to 2D by making one of the following assumptions, using the terminology in the paper by Kostli *et al.* [4]:

1. two-dimensional source distribution
2. two-dimensional source directivity
3. two-dimensional detector directivity

2D source distribution implies that the source is truly two-dimensional and it lies in the detection plane. This is not a very realistic scenario for biomedical applications since there are generally 3D sources present in the human body. The second assumption implies that even though the source is 3D, it is constant in the third direction. This kind of source will be highly directional and the signals received by the detector will only be from sources in the detection plane. The third assumption is relevant for highly directional detectors that are insensitive to signals coming from outside the detection plane. Thus a 2D cross-sectional slice of the unknown source is reconstructed and the image reconstruction problem is reduced to 2D. All three assumptions imply that detected acoustic signals are only from in-plane sources. However, these assumptions are not exactly equivalent. The first two assumptions impose constraints on the source geometry that may not exist. This limitation can affect the accuracy of the resulting 2D reconstructed image which may be especially important for quantitative optoacoustic imaging. In this paper, we consider the scenario based on the third assumption where the problem is reduced to 2D due to detector's directivity. This is achieved by using a linear array of anisotropic transducers which have tall, narrow elements that are essentially insensitive to out of plane acoustic waves.

There are several algorithms that have been proposed for 3D image reconstruction in OAT for measurements over a planar aperture. These include the Fourier-based algorithm [4–6], synthetic aperture (SA) algorithm [7, 8] synthetic aperture plus coherent weighting algorithm [9], and universal backprojection algorithm [10]. Some of these algorithms have also been applied to image reconstruction in 2D OAT. The Fourier based algorithm is theoretically exact in 3D for continuously sampled data on an infinite measurement aperture but not necessarily in 2D. This algorithm implicitly uses the second assumption above when applied in 2D, namely that the object is does not vary in the third direction. Synthetic aperture and coherent weighting algorithms [7–9], on the other hand, are approximate reconstruction algorithms. There exists an algorithm in reflection mode tomography that was proposed by Norton [11], which is theoretically exact in 2D for continuously sampled data on an infinite measurement aperture. We have applied this algorithm to OAT for the first time (to the best of our knowledge). We have implemented this algorithm for a planar geometry using a linear transducer array with tall, narrow elements.

Of course, no algorithm is theoretically exact for sampled data acquired on a finite interval, so this paper compares these algorithms for that practically relevant regime by examining image contrast, resolution and noise properties. The studies are performed using simulated optoacoustic pressure data. We go beyond the standard image quality metrics by computing noise texture measures like local noise power spectra (LNPS) and resolution measures like local modulation transfer function (LMTF). These noise and resolution measures are used to obtain the local noise equivalent quanta (LNEQ) metric that is known to predict signal detectability under certain conditions [12].

## 2. METHODS

The optoacoustic pressure signals,  $p(\mathbf{r}, t)$ , for an impulse optical illumination, are related to the absorbed optical energy  $A(\mathbf{r})$  [13] as

$$p(\mathbf{r}, t) = \eta \int d^3 r' A(\mathbf{r}') \frac{\partial}{\partial t} \frac{\delta(t - \frac{|\mathbf{r} - \mathbf{r}'|}{c})}{4\pi |\mathbf{r} - \mathbf{r}'|}, \quad (2)$$

where  $\eta = \frac{\beta}{C_p}$ . Eq. (2) states that the time integral of acoustic pressure at a point  $\mathbf{r}$  and time  $t$  is given by the integral of the absorbed optical energy function over a spherical surface of radius  $|\mathbf{r} - \mathbf{r}'| = ct$  centered at  $\mathbf{r}$ . A simple but inexact way to reconstruct  $A(\mathbf{r})$  is to spatially resolve the optoacoustic waves by using the speed of sound and to backproject them over hemispheres. In 2D geometry, this reduces to spatially resolving the optoacoustic waves by using the speed of sound and backprojecting over semicircles to obtain a two-dimensional slice of  $A(\mathbf{r})$ . This is the method followed by the synthetic aperture algorithm.

Let us consider a line of transducers along the  $x$  axis (i.e. at  $y = 0, z = 0$ ). Let  $A(x, z)$  represent an effective 2D slice of the absorbed optical energy function in the half-plane ( $y = 0, z > 0$ ). The pressure signals in 2D reduce to (as derived in appendix A)

$$p(x, z = 0, t) = \frac{\eta c}{4\pi} \int \int dx' dz' A(x', z') \frac{\partial}{\partial t} \delta \left( ct - \sqrt{(x - x')^2 + z'^2} \right). \quad (3)$$

Define  $g(x, t)$  as:

$$\begin{aligned}
g(x, t) &\equiv \frac{4\pi}{\eta c} \int p(x, t') dt' \\
&= \int \int dx' dz' A(x', z') \delta \left( ct - \sqrt{(x - x')^2 + z'^2} \right).
\end{aligned} \tag{4}$$

We will consider 3 algorithms for our study: an approach based on Norton's algorithm, the Fourier-based approach, and the synthetic aperture algorithm. We will not consider the synthetic aperture plus coherent weighting algorithm since it is non-linear due to the presence of the coherence factor, and nonlinear algorithms cannot be meaningfully characterized using the LMTF, LNPS and LNEQ functions.

## 2.1. Application of Norton's algorithm for reflection mode tomography to OAT

In this section we derive an exact expression for optoacoustic image reconstruction in 2D closely following derivation of an algorithm by Norton for reflection mode tomography [11].

Letting  $r \equiv ct$  and using the identity,  $\delta(r - a) = 2r\delta(r^2 - a^2)$ , one can write equation(4) as:

$$g(x, t) = 2r \int \int dx' dz' A(x', z') \delta(r^2 - (x - x')^2 - z'^2). \tag{5}$$

Defining new variables,  $\rho = r^2$ ,  $\zeta = z^2$ , and substituting in equation (5) yields

$$g(x, \rho) = \sqrt{\rho} \int \int dx' d\zeta' \frac{A(x', \sqrt{\zeta'})}{\sqrt{\zeta'}} \delta(\rho - (x - x')^2 - \zeta'). \tag{6}$$

Finally, setting

$$g'(x, \rho) = \frac{g(x, \sqrt{\rho})}{\sqrt{\rho}}, \tag{7}$$

and

$$A'(x, \zeta) = \frac{A(x, \sqrt{\zeta})}{\sqrt{\zeta}}, \tag{8}$$

, equation (6 ) becomes

$$g'(x, \rho) = \int dx' d\zeta' A'(x, \zeta) \delta(\rho - \zeta' - (x - x')^2), \tag{9}$$

which can be written as a 2D convolution,

$$g'(x, \rho) = A'(x, \rho) * * \delta(\rho - x^2). \tag{10}$$

This convolution relation can in principle be solved for  $A'$  by taking 2D Fourier transform on both sides of equation (10) with respect to  $x$  and  $\rho$ . The 2D convolution in Fourier space becomes multiplication of the 2D Fourier transforms due to the convolution-multiplication theorem. This can then be explicitly solved for the Fourier transform of  $A'$  and on taking the inverse 2D Fourier transform one obtains  $A'(x, \rho)$ . The transformation of  $g(x, t)$  into  $g'(x, \rho)$  by equation (7) can be regarded as a 1D geometric distortion of the  $x - r$  plane in the  $r$  direction. The double convolution relation, equation (10) implies that the time-integrated pressure signal is equivalent to a linear, space-variant mapping of the absorbed optical energy from points in the  $x - z$  object plane to hyperbolas in the  $x - r$  measurement plane (please see reference [11], section II for more details).

Another approach that is more direct to solving equation (10) is to seek a solution such that:

$$A'(x, \rho) = g'(x, \rho) * * R(x, \rho) \tag{11}$$

where we need to determine  $R(x, \rho)$ . This can be done using the method outlined in Norton's paper [11] and this is also derived in appendix B and the final result is:

$$A(x, z) = 2z\nu_c^2 \int \int g(x', r) R_1[\nu_c\{z^2 - r^2 + (x - x')^2\}] dr dx'. \quad (12)$$

where  $R_1(u) = 4\text{sinc}(2u) - 2\text{sinc}^2(u)$  and  $\nu_c$  is the cut-off frequency that dictates the band-limit of the measured signals.

The above relation is an exact equation relating the absorbed optical energy in the medium to a filtered back-projection of time-integrated pressure signals.

In the case when  $z \gg \nu_c^{-\frac{1}{2}}$ , this can be approximated as:

$$A(x, z) = z\nu_c^{\frac{3}{2}} \int \int \frac{g(x', r)}{r} R_1[\sqrt{\nu_c}\{\sqrt{z^2 + (x - x')^2} - r\}] dr dx'. \quad (13)$$

Defining  $G(x', r) \equiv \frac{g(x', r)}{r} * R_1[\sqrt{\nu_c}r]$  and substituting in Eq. (13) yields:

$$A(x, z) = z\nu_c^{\frac{3}{2}} \int G\left(x', \sqrt{z^2 + (x - x')^2}\right) dx'. \quad (14)$$

Equation (13) is similar to the filtered backprojection (FBP) expression used for image reconstruction in computer tomography (CT). The function  $R_1$  is the same as the Fourier transform of the truncated ramp filter used in the FBP expression [14]. Eq. (14) can be seen as backprojection of the filtered function  $G$ . So this algorithm is equivalent to 1D filtration at each transducer position  $x'$  followed by backprojection on circular arcs. Here,  $\nu_c^{-\frac{1}{2}}$  can be regarded as a measure of the resolution of signal  $g(x, r)$  in the temporal direction since  $\nu_c$  is the bandwidth of the function  $g'(x, \rho)$  with respect to the square of the temporal variable  $r$ . We found that the exact Norton's algorithm was extremely sensitive to the choice of cut-off frequency and did not give us good results. Hence, we implemented the approximate equation (13) as Norton-based algorithm.

So  $A(x, z)$  can be obtained via the following steps in the approximate Norton-based algorithm:

1. Convolve the 2D time-integrated pressure signal  $g$  with 1D filter  $R_1$  with respect to the temporal variable  $r$ .
2. Map the result onto a circular grid for a given  $(x, z)$ .
3. Sum the resulting expression over all the transducers.
4. Multiply the result by the distance from the transducer axis,  $z$  and other constant factors.

## 2.2. Fourier-based algorithm

This algorithm has been derived by Kostli *et al.* [4] and L.V.Wang *et al* [5]. It relates the Fourier transform of the absorbed optical energy function to the Fourier transform of the measured optoacoustic pressures. The relation in 2D is given by [4]:

$$A\left(k_x, k_z = \sqrt{\left(\frac{\omega}{c}\right)^2 - k_x^2}\right) = \frac{2c\sqrt{\omega^2 - c^2k_x^2}}{\omega} P(k_x, \omega) \quad (15)$$

where

$$P(k_x, \omega) = \int \int p(x, t) \exp(-ik_x x) \cos(\omega t) dx dt, \quad (16)$$

and  $\omega = c\sqrt{k_x^2 + k_z^2}$ . Note that our notation is different from that in reference [4].

Here,  $A(x, z)$  can be obtained via the following steps:

1. Take the real part Fourier transform of pressure,  $p(x, t)$  with respect to time.
2. Take the Fourier transform of the result with respect to  $x$ . This gives us  $P(k_x, \omega)$ .
3. Scale  $P(k_x, \omega)$  via equation (15) to obtain  $A\left(k_x, k_z = \sqrt{\left(\frac{\omega}{c}\right)^2 - k_x^2}\right)$ .

4. Map  $A(k_x, k_z = \sqrt{(\frac{\omega}{c})^2 - k_x^2})$  to a Cartesian grid via interpolation to obtain  $A(k_x, k_z)$ . We employed bilinear interpolation. Note that only values for which  $k_x^2 \leq (\frac{\omega}{c})^2$  are used in the mapping. Higher values would produce imaginary values of  $k_z$  (physically they correspond to rapidly decaying evanescent wave components).
5. Inverse Fourier transform  $A(k_x, k_z)$  to obtain  $A(x, z)$ .

### 2.3. Synthetic aperture based algorithm

This algorithm relates the signal intensity at each image point  $A(x, z)$  to the sum of signals from the transducer at different positions delayed with the time it takes the signal to travel from the transducer position to the point [8].

$$A(x, z) = \int g\left(x', \frac{\sqrt{(x-x')^2 + z^2}}{c}\right) dx' \quad (17)$$

So the steps involved for obtaining  $A(x, z)$  are:

1. For each point  $(x, z)$  in the source, sum over time-integrated pressure samples corresponding to transducer positions  $x'$  at different times  $t$  such that  $\sqrt{(x-x')^2 + z^2} = ct$ .

### 2.4. Details of the simulation

All the simulations were performed using 128 transducer positions spaced 0.1 mm apart and 128 time samples of width 67 ns. Time-integrated pressure data was simulated by integrating the optoacoustic source over circles of radii  $ct$  with the transducer placed at the center of these circles. Simulated 2D pressure data was used for the Fourier based algorithm while time-integrated simulated pressure data was used for the synthetic aperture and Norton based algorithms. In order to focus simply on the acquisition geometry and the inherent differences between the algorithms, we did not simulate a low pass or bandpass transducer response.

Simulated pressure data was generated for two different phantoms - a circular phantom and a phantom consisting of a line of rectangles. An exact analytical expression was used to generate the time-integrated pressure data for the circular and point source phantoms. A discrete numerical method was used to generate the time-integrated pressure data for the line phantom. This method is based on an implementation of a variation of Siddon's algorithm [15] for computing the intersection lengths of an arc specified by the coordinates of a source and receiver with a pixel. The circular phantom was of radius 1 mm with its center placed at a distance of 2 mm from the transducer axis. The line of rectangles was placed at a distance of 2 mm from the transducer axis with each rectangle being 0.5 mm x 0.3 mm wide. The images were constructed on a 128 x 128 grid.

To study the resolution, simulated pressure data was generated for a point source of size 0.1 mm (same as pixel width) placed at a distance of 1.0 mm from the transducer axis. A zoomed-in image of a point source was reconstructed using the 3 algorithms with a zoom factor of 10. The images were reconstructed on a 64x64 grid. We used these point source images to compute a local impulse response function (LIR). The LIR is a generalization of the point-spread function applicable when the image acquisition and reconstruction processes are not shift-invariant, as is the case here. We then computed the two-dimensional Fourier transforms of the LIRs to obtain what Barrett and Myers have called a local modulation transfer function (LMTF) [12]. A standard modulation transfer function (MTF) is the absolute value of the Fourier transform of the system's point spread function and predicts the ratio of output modulation to input modulation as a function of spatial frequency. Localized modulation transfer function (LMTF) is the generalization of MTF to linear, shift-variant systems. Higher and broader LMTF indicates better resolution properties.

Random Gaussian noise with mean 0 and a standard deviation of 1.0 was used for noisy pressure signals for the noise studies. Noisy images were constructed on a 64 x 64 grid using a zoom factor of 10. The noise studies were performed for 500 realizations. LNPS is a generalization of the noise power spectra (NPS) concept that can be used for linear systems without the assumption of shift invariance which does not hold for finite transducer aperture systems in OAT. LNPS was computed by first generating a set of 500 realizations of reconstructed images for each algorithm corresponding to pure Gaussian noise pressure. For each set of these reconstructed images, the mean image was computed. The mean image was



then subtracted from the other 500 images. LNPS was then obtained by taking the average squared modulus of the Fourier transform (FT) of the subtracted images:

$$LNPS = \frac{1}{N} \sum_{i=1}^N |FT(noisyImage(i) - meanImage)|^2,$$

where N is the number of realizations.

LNEQ is defined as the ratio of the square of the LMTF to the LNPS:

$$LNEQ = \frac{(LMTF)^2}{LNPS}$$

LNEQ is a kind of frequency-dependent signal-to-noise ratio generalized to linear, shift-variant systems. Higher LNEQ implies higher signal detectability performance for the so-called ideal observer in the task when both signal and background are known exactly [12].

### 3. RESULTS

#### 3.1. Phantom Images

In all the phantom images shown in this section, the transducer axis is along the bottom of the images. Figure 1 shows non-zoomed-in images produced by the 3 algorithms for a circular phantom of radius 1 mm placed at a distance of 2 mm from the transducer axis. The image reconstructed via the Fourier based algorithm has sharp edges but it is non-uniform and has lower contrast. The synthetic aperture image is quite blurred. The image reconstructed via Norton's approach is quite sharp and fairly uniform. Note that we observe two images in the Fourier-based algorithm due to the implicit symmetry assumption in the reconstruction. Figure 2 shows non-zoomed-in images of a line of small rectangles of size 0.5 mm x 0.3 mm placed at a distance of 2.0 mm from the transducer axis. The circular arc artifacts are more visible in the synthetic aperture algorithm than the Norton-based algorithm due to the additional filtration step that is performed in the Norton-based algorithm. In addition, the rectangles themselves are much sharper and more filled-in in the Norton-based algorithm compared to the other two algorithms.

#### 3.2. Spatial Resolution

The images of zoomed-in point sources are shown in figure 3, where the transducer axis is along the bottom of the images. The LIR plot for the 3 algorithms is shown in figure 4. These show that Fourier based algorithm shows the best resolution perpendicular to the transducer array while Norton's algorithm shows the best resolution parallel to the transducer array. The main difference between Norton's algorithm and the SA algorithm is filtering. This results in a much narrower LIR for Norton's algorithm than for the SA algorithm. In general, the lateral resolution for Norton-based and SA algorithms is much better than the depth resolution (perpendicular to the transducer axis). The full width at half-maxima (FWHM) results are shown in table 1.

Figure 5 shows the LMTF images for the three algorithms. The LMTF images exhibit an asymmetry due to the finite transducer length. The reciprocal relationship between LIR and LMTF is exhibited in these images. LMTF for SA algorithm is the narrowest since LIR for SA is the broadest. Figure 6 shows the LMTF plots. LMTF for Fourier based algorithm is the best in the direction perpendicular to the transducer axis, especially for smaller frequencies. Norton's Algorithm produces the best LMTF profile in the lateral direction which is expected since it had the smallest lateral resolution.

### 3.3. Noise texture

The noise texture images are simply images of a uniform background reconstructed from pressure signals to which zero mean Gaussian noise has been added. Figure 7 shows the noise texture in the unzoomed images reconstructed via the three algorithms. The noise in the Fourier and Norton-based algorithms seems uniformly speckled while the smeared out noise texture in SA algorithm seems to exhibit some long range correlations. Such 'blobbiness' in the noise can impede detectability of signals of size comparable to the blob size. LNPS describes the frequency content of the background texture in the region surrounding the location of the signal in the image [12]. Figure 8 shows the zoomed-in (250%) images of LNPS for the three algorithms. LNPS images for Norton-based and synthetic aperture algorithms are pretty symmetric. But it is not so for Fourier-based algorithm. Note that the input to the Fourier-based algorithm was Gaussian noise pressure while the input to the other two algorithms was time-integrated Gaussian noise pressure, which introduces noise correlations that can affect the form of the LNPS. Figure 9 shows the LNPS plots in the two directions. The plot for SA algorithm was omitted because it was several orders of magnitude higher than the other two algorithms and could not be fit into the same plot. The shapes for LNPS are very different for Norton-based and Fourier-based algorithms.

### 3.4. Signal Detectability/LNEQ

Figure 10 shows the zoomed-in (250%) images of LNEQ for the three algorithms. Figure 11 shows the LNEQ plots. In general, LNEQ images are somewhat difficult to interpret visually, as they represent a kind of generalized frequency-domain detectability transfer function, but bright areas correspond to frequency components that are more likely to be detected against a background of correlated noise, as captured by the LNPS. To calculate the so-called ideal observer signal to noise ratio for a small low contrast signal, one would calculate the squared magnitude of the Fourier transform of the signal, multiply it by the LNEQ shown in the images, and integrate over all frequencies. The plots in Fig. 11 give a better sense of the relative magnitude of the LNEQ for the different algorithms. Higher values are better and the Norton-based algorithm produces the highest LNEQ in both directions followed by the Fourier-based algorithm. This indicates superior ideal observer signal detectability in images reconstructed by the use of the Norton-based algorithm. For all algorithms the LNEQ becomes small at  $5 \text{ mm}^{-1}$  in the depth direction and  $7 \text{ mm}^{-1}$  in the lateral direction.

## 4. DISCUSSION

The 2D geometry that we consider in this paper reduces the inherently 3D optoacoustic image reconstruction to 2D due to transducer's 2D directivity. This results in the measured 2D optoacoustic signal being related to the time derivative of the integral of the absorbed optical energy over circular arcs centered at the transducer as given by eqn. 3. The three algorithms considered here for evaluation have some intrinsic differences. The SA algorithm is approximate to start with and involves only the delay and sum technique based on backprojection over circular arcs. The Norton-based algorithm improves on SA algorithm by providing a filtration step that filters the time-integrated pressure data before using the backprojection over circular arcs technique. The Fourier-based algorithm is not exact in the 2D geometry that we are considering since it assumes that the optoacoustic source is constant in the third dimension. These intrinsic differences in the algorithms explain the differences in sharpness and quality of the reconstructed images.

Norton-based and SA algorithms use time-integrated pressure as input signal while the Fourier-based algorithm uses pressure signal as input. Integration of noisy data introduces noise correlations that can affect the LNPS. This was reflected in the blobbiness of the noise texture images of the SA algorithm. The additional filtration step in the Norton-based algorithm aids in the removal of such blobbiness and gives a much better noise texture. The Fourier-based algorithm does not show such blobbiness in noise texture.

## 5. CONCLUSIONS

We explored three different ways in which a 2D image can be reconstructed in OAT. We implemented and evaluated three algorithms for 2D image reconstruction in OAT- Fourier-based, Norton-based and synthetic aperture algorithms. We found that the 2D Fourier-based algorithm offers better resolution and LMTF in the depth direction while Norton's algorithm offers the best lateral resolution. However, we found that in reconstructions of phantoms the images produced by Norton-based algorithm looked the sharpest and more uniform. The LNEQ data suggests that Norton-based algorithm has the best signal detectability.

## ACKNOWLEDGMENTS

This work was supported in part by the University of Chicago's SPORE grant for breast cancer research, a DoD breast cancer pre-doctoral fellowship (W81XWH-08-1-0331) and an American Cancer Society Research Scholar award. D.M. would like to thank Phillip A. Vargas for implementing the forward model in 2D for OAT and for helpful discussions related to it.

## 6. APPENDIX

### A. 2D relation between pressure and absorbed optical energy function

Starting with equation (2),

$$\begin{aligned} p(\mathbf{r}, t) &= \eta \int d^3 r' A(\mathbf{r}') \frac{\partial}{\partial t} \frac{\delta(t - \frac{|\mathbf{r} - \mathbf{r}'|}{c})}{4\pi |\mathbf{r} - \mathbf{r}'|} \\ &= \frac{\eta c}{4\pi} \frac{\partial}{\partial t} \int_{|\Delta \mathbf{r} = ct} \frac{A(\mathbf{r}')}{ct} dS', \end{aligned} \quad (18)$$

where  $\Delta \mathbf{r} = |\mathbf{r} - \mathbf{r}'|$ ,  $dS'$  is the differential surface area and the integral is over a spherical surface centered on  $\mathbf{r}$  and of radius  $\Delta \mathbf{r}$ . This can be written as:

$$p(\mathbf{r}, t) = \frac{\eta c}{4\pi} \frac{\partial}{\partial t} \int_{|\Delta \mathbf{r} = ct} (ct)^2 \frac{A(\mathbf{r}')}{ct} d\Omega',$$

where  $d\Omega' = \sin \theta' d\theta' d\phi'$  is the solid angle. This equation in 2D ( $x - z$  plane) reduces to:

$$p(x, z, t) = \frac{\eta c}{4\pi} \frac{\partial}{\partial t} \int_{|\rho - \rho'| = ct} (ct) A(\rho') d\phi', \quad (19)$$

where  $\rho = \sqrt{x^2 + z^2}$ , is the polar radial coordinate.

Using the integral property of delta functions, this can be written in polar coordinates as:

$$p(x, z, t) = \frac{\eta c}{4\pi} \frac{\partial}{\partial t} \int \int_{|\rho - \rho'| = ct} |\rho - \rho'| d(|\rho - \rho'|) \delta(ct - |\rho - \rho'|) A(\rho') d\phi'. \quad (20)$$

This can be written equivalently in 2D Cartesian coordinates as:

$$p(x, z, t) = \frac{\eta c}{4\pi} \frac{\partial}{\partial t} \int \int dx' dz' A(x', z') \delta \left( ct - \sqrt{(x - x')^2 + z'^2} \right).$$

### B. Derivation of Norton-based algorithm

In this section, we shall derive Eq. (12) following the method detailed in Norton's paper [11]. Define the Fourier transform with respect to  $r$  as:

$$\tilde{f}(x, \nu) = \int f(x, r) \exp(i2\pi \nu r) dr. \quad (21)$$

Taking the Fourier transform of equation (10) on both sides with respect to  $\rho = r^2$  we get

$$\tilde{g}'(x, \nu) = \tilde{A}'(x, \nu) * \exp(i2\pi x^2 \nu). \quad (22)$$

On convolving both sides with  $\exp(-i2\pi x^2\nu)$  we get

$$\tilde{g}'(x, \nu) * \exp(-i2\pi x^2\nu) = \tilde{A}'(x, \nu) * \exp(i2\pi x^2\nu) * \exp(-i2\pi x^2\nu), \quad (23)$$

where the convolution is with respect to  $x$ . Using the identity

$$\begin{aligned} \exp(i2\pi x^2\nu) * \exp(-i2\pi x^2\nu) &= \delta(2\nu x) \\ &= \left( \frac{\delta(x)}{2|\nu|} + \frac{\delta(\nu)}{2|x|} \right), \end{aligned}$$

equation (23) becomes

$$\begin{aligned} \tilde{g}'(x, \nu) * \exp(-i2\pi x^2\nu) &= \tilde{A}'(x, \nu) * \left( \frac{\delta(x)}{2|\nu|} + \frac{\delta(\nu)}{2|x|} \right) \\ &= \frac{1}{2|\nu|} \tilde{A}'(x, \nu) + \frac{1}{2} \delta(\nu) \left( \tilde{A}'(x, \nu) * \frac{1}{|x|} \right). \end{aligned} \quad (24)$$

Solving for  $\tilde{A}'(x, \nu)$  gives,

$$\tilde{A}'(x, \nu) = 2|\nu| \tilde{g}'(x, \nu) * \exp(-i2\pi x^2\nu) - |\nu| \delta(\nu) \left( \tilde{A}'(x, \nu) * \frac{1}{|x|} \right).$$

Using the identity  $|\nu| \delta(\nu) = 0$  to eliminate the second term on the right and taking the inverse Fourier transform ( $FT^{-1}$ ) with respect to  $\nu$  on both sides one finds

$$A'(x, \rho) = g'(x, \rho) * FT^{-1}\{2|\nu| \exp(-i2\pi x^2\nu)\}_\rho. \quad (25)$$

Comparing Eq. (25) with Eq.(11), we see that

$$\begin{aligned} R(x, \rho) &= FT^{-1}\{2|\nu| \exp(-i2\pi x^2\nu)\}_\rho \\ &= 2FT^{-1}\{|\nu|\}_\rho + x^2 \end{aligned} \quad (26)$$

If the data  $S'(x, \nu)$  is bandlimited by a cut-off frequency  $\nu_c$ , then the above convolution relation is unchanged if we impose the same bandlimit on  $R(x, \rho)$ . So one gets:

$$R(x, \rho) = 2FT^{-1} \left\{ |\nu| \text{rect} \left( \frac{\nu}{2\nu_c} \right) \right\}_{\rho+x^2}. \quad (27)$$

One can write out the convolution in equation (25) as

$$A'(x, \rho) = \nu_c^2 \int \int g'(x', \rho) R_1[\nu_c(\zeta - \rho + (x - x')^2)] d\rho dx',$$

where  $R_1(u) = 4\text{sinc}(2u) - 2\text{sinc}^2(u)$ .

Substituting for  $A'(x, \rho)$ ,  $S'(x, \rho)$  and for  $\zeta$  and  $\rho$ , one obtains

$$A(x, z) = 2z\nu_c^2 \int \int g(x', r) R_1[\nu_c(z^2 - r^2 + (x - x')^2)] dr dx', \quad (28)$$

which is the desired result.

## REFERENCES

1. R. A. Kruger, D. R. Reinecke, and G. A. Kruger, "Thermoacoustic computed tomography—technical considerations," *Med Phys* **26**, pp. 1832–1837, Sep 1999.
2. M. Xu and L. V. Wang, "Photoacoustic imaging in biomedicine," *Rev. Sci. Instr.* **77**, pp. 041101–1–041101–22, Apr 2006.
3. R. A. Kruger, P. Liu, Y. R. Fang, and C. R. Appledorn, "Photoacoustic ultrasound (PAUS)—reconstruction tomography," *Med Phys* **22**, pp. 1605–1609, Oct 1995.
4. K. P. Kostli and P. C. Beard, "Two-dimensional photoacoustic imaging by use of Fourier-transform image reconstruction and a detector with an anisotropic response," *Appl Opt* **42**, pp. 1899–1908, Apr 2003.
5. Y. Xu, D. Feng, and L. V. Wang, "Exact frequency-domain reconstruction for thermoacoustic tomography—I: Planar geometry," *IEEE Trans Med Imaging* **21**, pp. 823–828, Jul 2002.
6. K. P. Kostli, M. Frenz, H. Bebie, and H. P. Weber, "Temporal backward projection of optoacoustic pressure transients using fourier transform methods," *Phys Med Biol* **46**, pp. 1863–1872, Jul 2001.
7. C. G. A. Hoelen and F. F. M. de Mul, "Image Reconstruction for Photoacoustic Scanning of Tissue Structures," *Appl Opt* **39**, pp. 5872–5883, Nov 2000.
8. D. Feng, Y. Xu, G. Ku, and L. V. Wang, "Microwave-induced thermoacoustic tomography: reconstruction by synthetic aperture," *Med Phys* **28**, pp. 2427–2431, Dec 2001.
9. C. K. Liao, M. L. Li, and P. C. Li, "Optoacoustic imaging with synthetic aperture focusing and coherence weighting," *Opt Lett* **29**, pp. 2506–2508, Nov 2004.
10. M. Xu and L. V. Wang, "Universal back-projection algorithm for photoacoustic computed tomography," *Phys Rev E Stat Nonlin Soft Matter Phys* **71**, p. 016706, Jan 2005.
11. S. J. Norton, "Reconstruction of a reflectivity field from line integrals over circular paths," *J. Acoust. Soc. Am.* **67**, pp. 853–863, Mar 1980.
12. H. H. Barrett and K. J. Myers, *Foundations of Image Science*, pp. 1224–1225. Wiley Interscience, Hoboken, 2004.
13. M. Xu, Wang, and L. V, "Time domain reconstruction for thermoacoustic tomography in a spherical geometry," *IEEE Trans Med Imaging* **21**, pp. 814–822, Jul 2002.
14. A. C. Kak and M. Slaney, *Principles of Computerized Tomography Imaging*, pp. 71–72. IEEE Press, New York, 1988.
15. R. L. Siddon, "Fast calculation of the exact radiological path for a three-dimensional CT array," *Med. Phys.* **12**, pp. 252–255, 1985.

FWHM	Fourier-based	Norton-based	Synthetic Aperture
Depth (mm)	0.154	0.200	0.471
Lateral (mm)	0.161	0.151	0.189

**Table 1.** FWHM values for a point source of size 0.1 mm with pixel width=0.1 mm

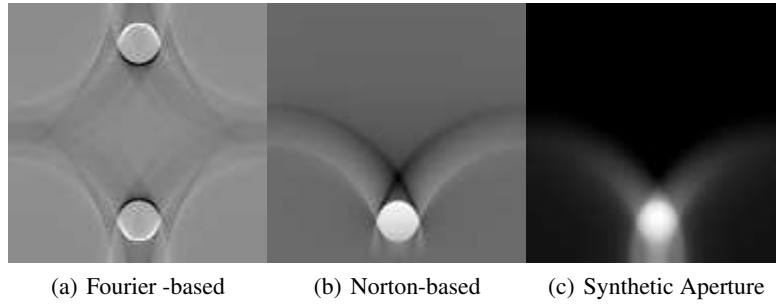


**Figure 1.** Circular phantom images

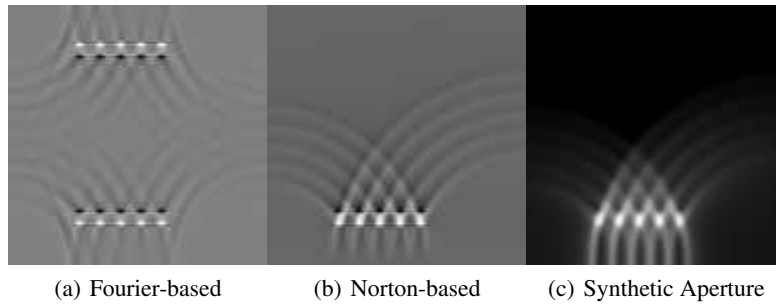


**Figure 2.** Images of a line of rectangles

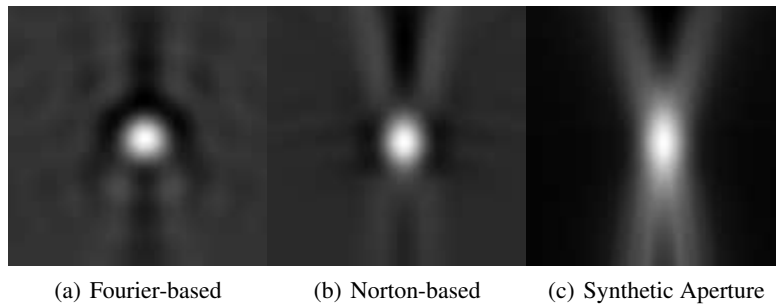


**Figure 3.** Zoomed-in point source images

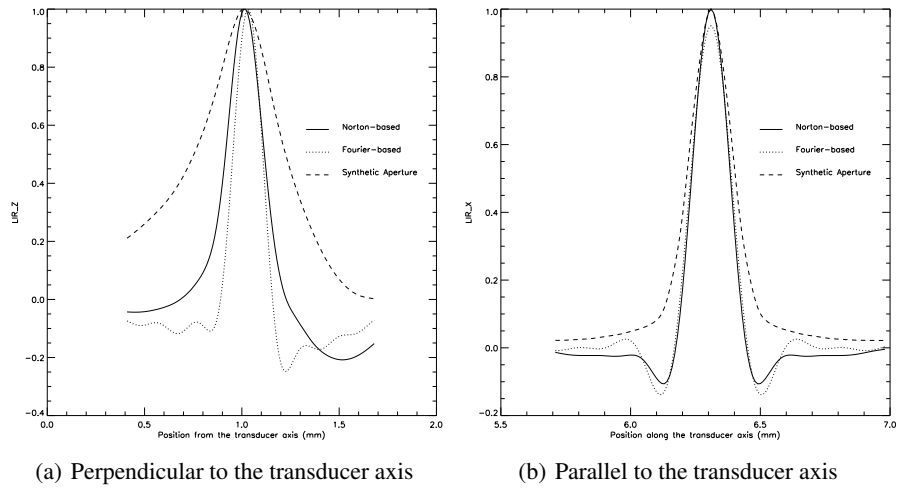


**Figure 4. LIR Plots**

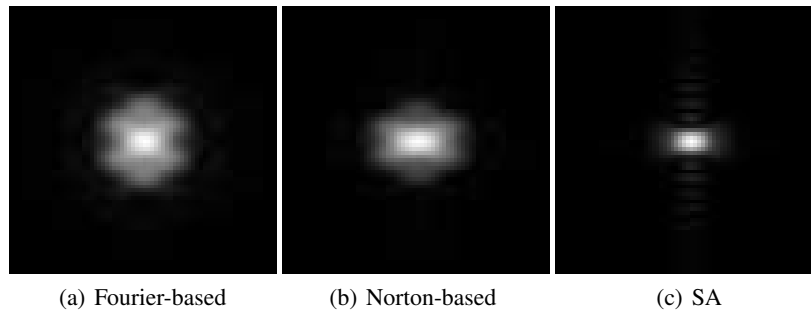


**Figure 5. Zoomed-in LMTF Images**

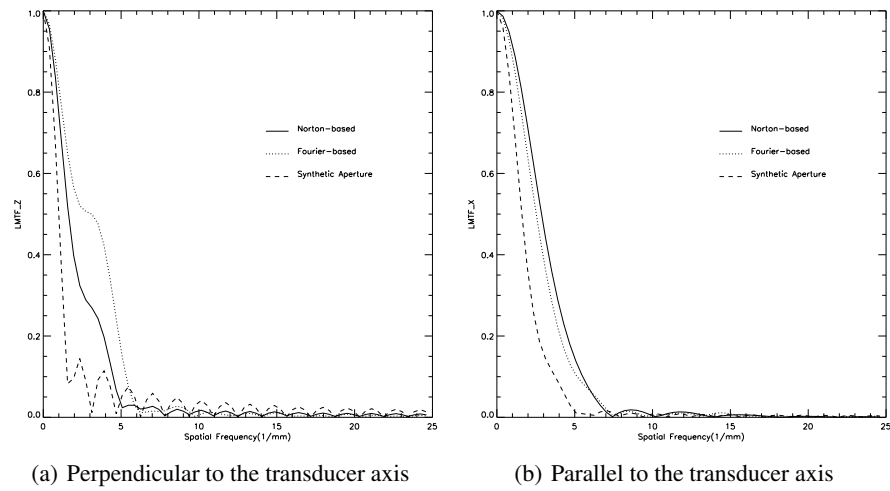


**Figure 6. LMTF plots**

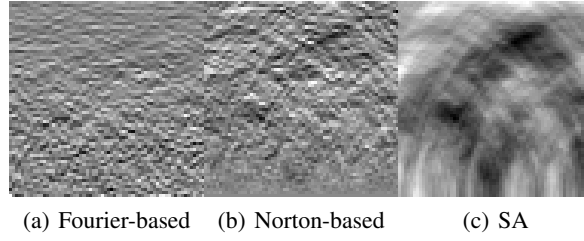


**Figure 7.** Noisy images

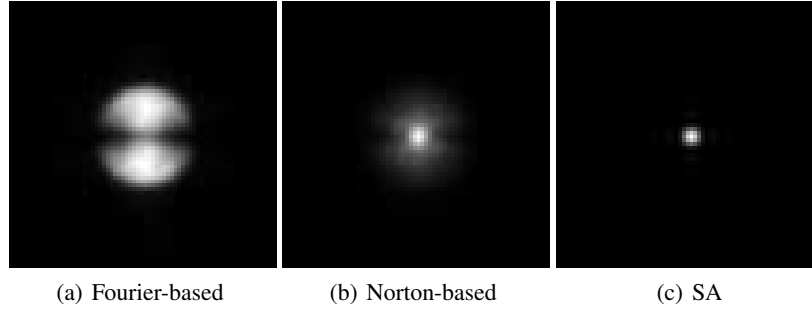


**Figure 8.** Zoomed-in LNPS Images

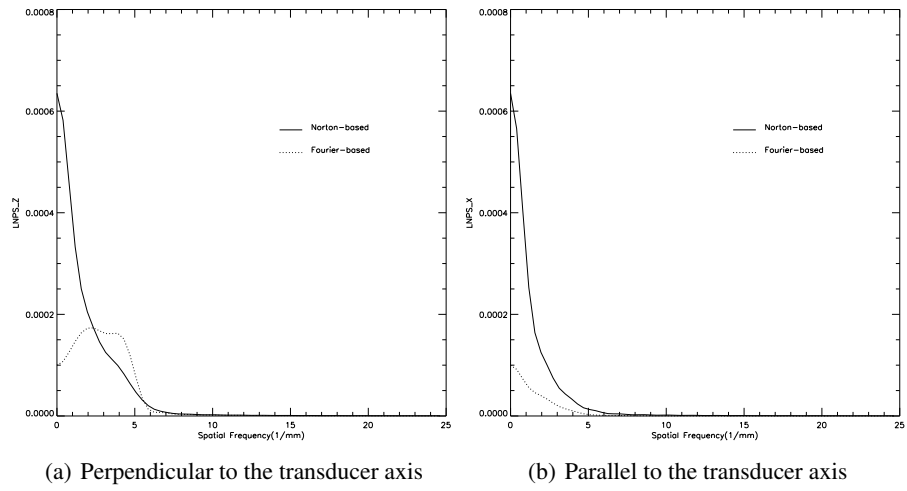


**Figure 9.** LNPS Plots

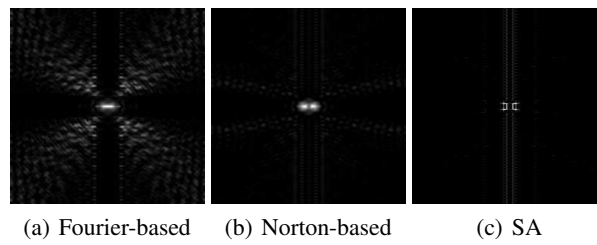
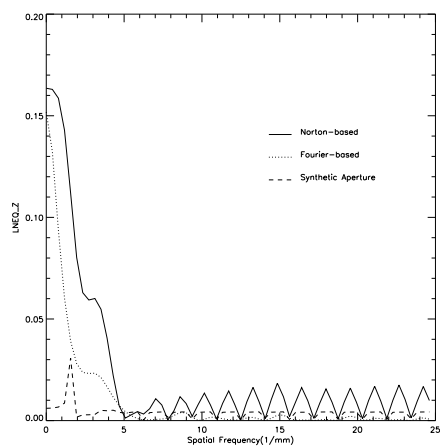
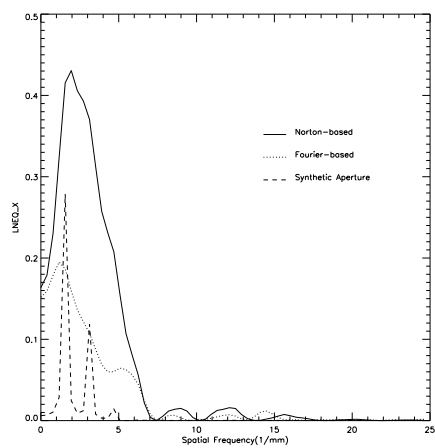


**Figure 10.** LNEQ Images





(a) Perpendicular to the transducer axis



(b) Parallel to the transducer axis

**Figure 11. LNEQ Plots**

# Image reconstruction in photoacoustic tomography with variable speed of sound using a higher-order geometrical acoustics approximation

Dimple Modgil\*, Mark A. Anastasio, Kun Wang and Patrick J. La Rivière\*

\* Department of Radiology, The University of Chicago,  
Department of Biomedical Engineering, Illinois Institute of Technology

## ABSTRACT

Previous research correcting for variable speed of sound in photoacoustic tomography (PAT) has used a generalized radon transform (GRT) model. In this model, the pressure is related to the optical absorption, in an acoustically inhomogeneous medium, through integration over non-spherical isochronous surfaces. This model assumes that the path taken by acoustic rays is linear and neglects amplitude perturbations to the measured pressure. We have derived a higher-order geometrical acoustics (GA) expression, which takes into account the first-order effect in the amplitude of the measured signal and higher-order perturbation to the travel times. The higher-order perturbation to travel time incorporates the effect of ray bending. Incorrect travel times can lead to image distortion and blurring. These corrections are expected to impact image quality and quantitative PAT. We have previously shown that travel-time corrections in 2D suggest that perceivable differences in the isochronous surfaces can be seen when the second-order travel-time perturbations are taken into account with a 10% speed of sound variation. In this work, we develop iterative image reconstruction algorithms that incorporate this higher-order GA approximation assuming that the speed of sound map is known. We evaluate the effect of higher-order GA approximation on image quality and accuracy.

**Keywords:** Optoacoustic tomography, photoacoustic tomography, thermoacoustic tomography, image reconstruction, variable speed of sound, inhomogeneous, travel times, geometrical acoustics,

## 1. INTRODUCTION

Optoacoustic imaging is a hybrid imaging technique that has attracted a lot of attention in recent years. It is based on the photoacoustic/optoacoustic effect which refers to acoustic wave generation upon absorption of pulsed optical energy by a medium. A slight rise in temperature of the medium due to the absorption of the incident electromagnetic wave results in thermoelastic expansion. This thermoelastic expansion and then contraction due to the pulsed electromagnetic waves leads to the generation of acoustic waves. Under the constraints of thermal and stress confinement, this thermal expansion leads to a rise in pressure,  $p(\mathbf{r}, t)$ , that satisfies the three-dimensional inhomogeneous wave equation [1]:

$$\frac{\partial^2 p(\mathbf{r}, t)}{\partial t^2} - c^2 \nabla^2 p(\mathbf{r}, t) = \frac{\beta}{C_p} \frac{\partial}{\partial t} H(\mathbf{r}, t), \quad (1)$$

where  $H(\mathbf{r}, t)$ , the heating function, is the thermal energy deposited by the electromagnetic radiation per unit time per unit volume,  $\beta$  is the isobaric volume expansion coefficient and  $C_p$  is the specific heat of the medium. The heating function can be expressed as the product of a spatially varying optical absorption function of the medium,  $A(\mathbf{r})$ , and a time dependent optical illumination function,  $I(t)$ . Using standard Green's function techniques, the measure pressure signal can be related to the optical absorption function, assuming delta pulse illumination, as:

$$p(\mathbf{r}, t) = \eta \int d^3 r' A(\mathbf{r}') \frac{\partial}{\partial t} \frac{\delta(t - \frac{|\mathbf{r} - \mathbf{r}'|}{c})}{4\pi |\mathbf{r} - \mathbf{r}'|}, \quad (2)$$

where  $\eta = \frac{\beta}{C_p}$ . Eqn. (2) states that the time integral of acoustic pressure at a point  $\mathbf{r}$  and time  $t$  is given by the integral of the optical absorption function over a spherical surface of radius  $|\mathbf{r} - \mathbf{r}'| = ct$  centered at  $\mathbf{r}$ . A simple but inexact

---

Send correspondence to: Dimple Modgil, email: dimple@uchicago.edu

way to reconstruct  $A(\mathbf{r})$  is to spatially resolve the optoacoustic waves by using the speed of sound and to backproject time-integrated pressure signals over hemispheres.

This backprojection assumes that the speed of sound in the medium is constant and known. However, both these assumptions are not valid in tissues. Speed of sound in tissues can vary from 1350 m/s (in fat) to about 1700 m/s (for skin) for ultrasound waves in the 1-10 MHz range [2]. Using a constant speed of sound in image reconstruction can result in image distortion and poor image quality. There has been some work done previously to address the effect of speed of sound variations in OAT. Xu and Wang [3] [4] looked at variable speed of sound reconstruction in breast thermoacoustic tomography (TAT). They concluded that there is minor amplitude distortion in breast TAT and that variation in travel time is a first-order perturbation in a weakly acoustically heterogeneous medium. Zhang and Anastasio [5] derived a heuristic method for reconstructing acoustic speed and optical absorption distributions in a step-wise manner. Their work was also based on the first-order travel time effect. Kolkman *et al.* [6] devised a method to determine the speed of sound in tissue using two concentric rings based photoacoustic sensor based on first-order travel time effect. Manohar *et al.* [7] also devised a new and improved method to determine speed of sound using a photoacoustic imager. Agravonsky and Kuchment [8] have recently derived an analytic reconstruction formula for OAT for arbitrary detector geometry, such that the point detectors are placed on a closed surface and for variable speed of sound. Their analytic formula leads to reconstruction in terms of eigenfunction expansion. Zhen *et al.* [9] devised an iterative reconstruction algorithm, using finite-element method, that incorporates both attenuation and variable speed of sound.

Previous work on the speed of sound variation that is based on the generalized radon transform (GRT) model has only looked at the first-order effect of variable speed of sound [4] [5] [6]. In the GRT model the pressure is given by:

$$p(\mathbf{r}, t) = \eta \int d^3r' A(\mathbf{r}') \frac{\partial}{\partial t} \frac{\delta(t - \tau(\mathbf{r}, \mathbf{r}'))}{4\pi|\mathbf{r} - \mathbf{r}'|}, \quad (3)$$

where  $\tau(\mathbf{r}, \mathbf{r}')$  is the travel time for the sound wave to travel between points  $\mathbf{r}$  and  $\mathbf{r}'$ . It was assumed that sound rays continue to travel in straight line in the presence of acoustic heterogeneity and the travel-time between points  $\mathbf{r}$  and  $\mathbf{r}'$  is given as a line integral over the slowness map:

$$\tau(\mathbf{r}, \mathbf{r}') = \int_{\mathbf{r}_0} ds/c(s), \quad (4)$$

where  $\mathbf{r}_0$  is the straight line joining the points  $\mathbf{r}$  and  $\mathbf{r}'$ ,  $ds$  is the differential length element along that line and  $c(s)$  is the variable speed of sound. The effect of variable speed of sound on signal amplitude was neglected. Previous work based on the GRT model does not incorporate the effect of ray bending which may be significant when the speed of sound varies by 10% or more.

In this work, we investigate a higher-order geometrical acoustic approximation that incorporate first-order effect on the signal amplitude and higher-order effect on the travel times. We use this higher order approximation to construct the system matrix. We then iteratively reconstruct the images using third-order, second-order, first-order and zeroth-order travel time effects. We show that the higher-order GA approximation offers much better image quality and accuracy when the speed of sound varies by 10% or more.

## 2. METHODS

We treat the variation in the speed of sound as a perturbation to the background sound speed,  $c_0$ .

$$c(\mathbf{r}) = c_0 + \epsilon c_1(\mathbf{r}), \quad (5)$$

where  $\epsilon$  characterizes the magnitude of the perturbation.

## 2.1. Derivation of Geometrical Acoustics Approximation

The GA approximation ignores diffraction effects. It is valid in the short wavelength regime when the size of the inhomogeneity is much greater than the wavelength. In a scattering medium, this approximation is valid when the speed of sound does not change significantly over one wavelength. The Green's function in the acoustically inhomogeneous medium can be written as:

$$G(\mathbf{r}, \mathbf{r}', \omega) = g_0(\mathbf{r}, \mathbf{r}') \exp(i\omega\tau(\mathbf{r}, \mathbf{r}')), \quad (6)$$

where  $\tau$  is known as the eikonal function. The GA approximation gives us the eikonal equation in the limit  $\lambda \rightarrow 0$ :

$$[\nabla_{\mathbf{r}}\tau(\mathbf{r}, \mathbf{r}')] = c^{-2}(\mathbf{r}), \quad (7)$$

The eikonal equation implies:

$$\tau(\mathbf{r}, \mathbf{r}') = \int_{\mathbf{r}'}^{\mathbf{r}} ds/c(s), \quad (8)$$

where  $s$  denotes the arc length along the path between the points  $\mathbf{r}$  and  $\mathbf{r}'$  as shown in figure 1. Note that the curve connecting the points  $\mathbf{r}$  and  $\mathbf{r}'$  need not be a straight line. The ray trajectory is determined by the path that minimizes the acoustic path length (Fermat's principle) or equivalently, that minimizes the travel-time. For an acoustically homogeneous medium, this is a straight line. Previous work by Snieder *et al.* [10] concludes that to first-order in perturbation, this trajectory can be chosen to be the path along the reference ray that satisfies the eikonal equation (assuming the variation in speed of sound is slowly varying).

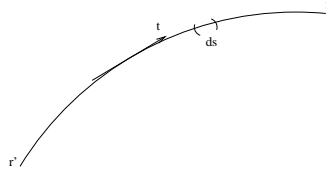


**Figure 1.** The path travelled by sound wave between points  $\mathbf{r}$  and  $\mathbf{r}'$ .

Using Eqn. (6), the pressure is given by:

$$p(\mathbf{r}, \omega) \simeq -i\omega\eta \int d^3r' A(r') g_0(\mathbf{r}, \mathbf{r}') \exp(i\omega\tau(\mathbf{r}, \mathbf{r}')), \quad (9)$$

Taking Fourier transform with respect to  $\omega$  we obtain the generalized radon transform (GRT):

$$p(\mathbf{r}, t) \simeq \eta \int d^3r' A(r') g_0(\mathbf{r}, \mathbf{r}') \frac{d}{dt} \delta(t - \tau(\mathbf{r}, \mathbf{r}')). \quad (10)$$

To zeroth-order, the amplitude is given by:

$$g_0(\mathbf{r}, \mathbf{r}') = \frac{1}{4\pi|\mathbf{r} - \mathbf{r}'|} \quad (11)$$

Using this expression for  $g_0(\mathbf{r}, \mathbf{r}')$ , we'll obtain the following expression for pressure:

$$p(\mathbf{r}, t) \simeq \eta \int d^3r' \frac{A(\mathbf{r}')}{4\pi|\mathbf{r} - \mathbf{r}'|} \frac{d}{dt} \delta(t - \tau(\mathbf{r}, \mathbf{r}')). \quad (12)$$

This expression along with the travel time given by Eqn. (4) is what has been used in the previous work addressing speed of sound variation based on the GRT model.

## 2.2. Higher-order Geometrical Acoustics Approximation

We can improve the first-order GA model by incorporating higher order effects on the amplitude and travel times.

- **Improvements to amplitude** - The first-order correction to the amplitude of the Green's function is given by:

$$g_0(\mathbf{r}, \mathbf{r}') = \frac{1}{4\pi|\mathbf{r} - \mathbf{r}'|} \sqrt{\frac{c(\mathbf{r})}{c(\mathbf{r}')}} \quad (13)$$

- **Improvements to the eikonal** - We can incorporate the effect of ray bending by considering the higher order perturbations in the eikonal. The assumption for first-order GA is that the speed of sound is slowly varying so that the time of travel can be obtained using linear rays. However, if this assumption is not true, it can lead to higher-order perturbations in travel times. Higher-order travel time perturbations contribute to ray bending. Following the methodology of Snieder *et al.* [10], perturbations in travel-time can be written as :

$$\tau(\mathbf{r}, \mathbf{r}') = \tau_0(\mathbf{r}, \mathbf{r}') + \epsilon\tau_1(\mathbf{r}, \mathbf{r}') + \epsilon^2\tau_2(\mathbf{r}, \mathbf{r}') + \dots, \quad (14)$$

where  $\epsilon$  is a small parameter.

Let  $\mathbf{r}_0$  denote the reference ray associated with the reference eikonal  $\tau_0(\mathbf{r}, \mathbf{r}') = \int_{\mathbf{r}_0} ds/c_0$ . Let the reference ray be parametrized by the variable  $s$  so that  $\mathbf{r}_0 = s\hat{\mathbf{t}}_0$ , where  $\hat{\mathbf{t}}_0$  is the unit vector along the reference ray. The first- and second-order perturbations to travel time are given by :

$$\tau_1(\mathbf{r}, \mathbf{r}') = - \int_{\mathbf{r}_0} \frac{c_1(s)}{c_0^2} ds, \quad (15)$$

and

$$\tau_2(\mathbf{r}, \mathbf{r}') = \int_{\mathbf{r}_0} \frac{c_0}{2} \left( \frac{c_1^2(s)}{c_0^4} - |\nabla\tau_1(\mathbf{r}, \mathbf{r}')|^2 \right) ds \quad (16)$$

The higher-order perturbations to travel times can be easily derived as described by Snieder *et al.* [10]. Thus, one can calculate the perturbed time of flight using these equations if one knows the reference ray. Note that this perturbation theory approach only works if the non-linear perturbations are small and there is no multipathing. Thus, we can obtain a higher-order estimate of the pressure than that given by Eqn. (12) by using Eqn. (13) for amplitude and keeping up to higher-order terms in Eqn. (14) and using these in Eqn. (10).

## 2.3. Details of the simulation

### 2.3.1. Travel time calculations

Travel times were calculated using up to fourth-order correction for different pixels for a specific transducer position. This was done in 2D for a 50x50 grid for a specific speed of sound map shown in figure 2. The blurred elliptical region (2 mm by 1.4 mm) in this map has the variable speed of sound with respect to the background. The background speed of sound was set to 1500 m/s. Curves of constant times were reconstructed using up to second-order travel times. This was done for a 5%, 10% and 15% speed of sound variation. The pixel size was set to 0.01 cm. The time sampling interval was set to 33.33 ns. The transducers were assumed to lie on a line to the left of the phantom 0.01 cm apart.

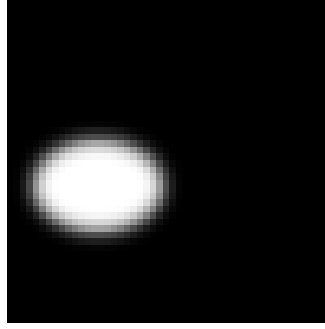


**Figure 2.** Speed of sound map

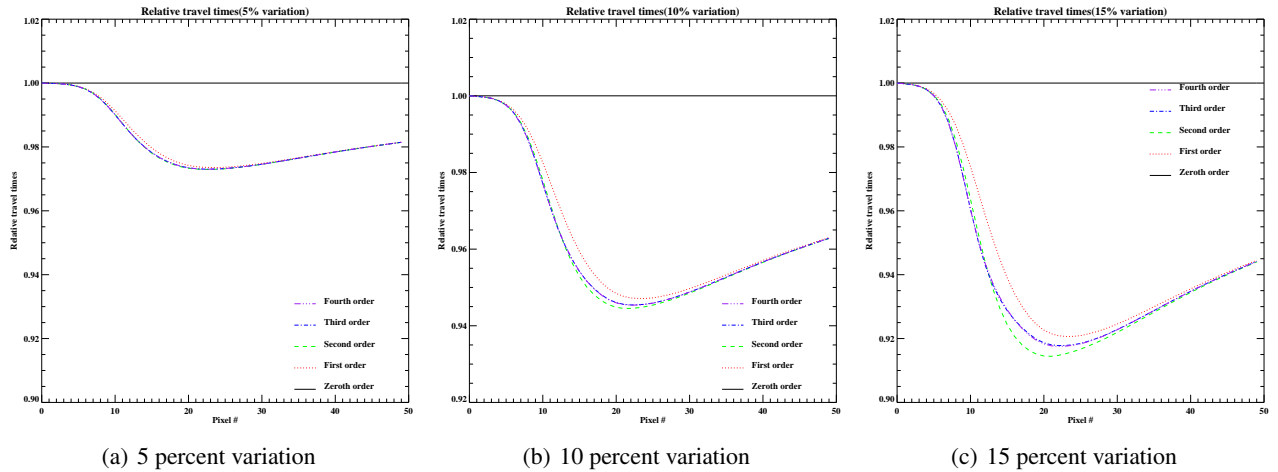
### 2.3.2. Image Reconstruction

The system matrices were constructed in 2D incorporating zeroth-order, first-order, second-order and fourth-order travel time effects. The images were then reconstructed iteratively using least-squares method. The conjugate gradient method. was used to choose the step direction for each iteration. The fourth-order travel time system matrix was used for the forward model. The images were then reconstructed iteratively using third-order, second-order, first-order and zeroth-order matrices. The image reconstruction was done on a 50x50 grid with parameters as specified above.

## 3. RESULTS

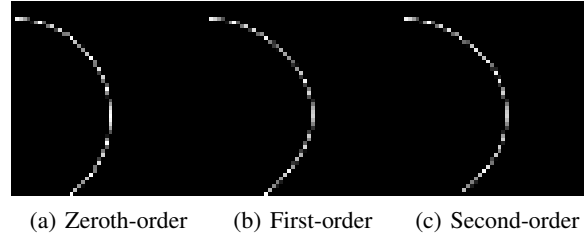
### 3.1. Isochrons and relative travel times

Figure 3 depicts the change to relative travel times for pixels located along the line (0, 1.0 mm) with the transducer placed at (0, 2.3 mm) in pixel coordinates. One observes that the higher-order travel time corrections become perceivable when the speed of sound varies by 10% or more. One can also see that the travel time perturbations seem to converge when one goes up to the third-order term. This suggests that one should use up to third-order travel time corrections in the forward model to most accurately represent the signal.



**Figure 3.** Relative travel times for transducer at (0, 2.3 mm) for phantom pixels along the line (0,1.0 mm) for a specific speed of sound map

Figures 4 and 5 depict the isochrons for the speed of sound map shown in figure 2 with the transducer placed at (0, 2.0 mm) and for a travel time of 1.665 micro-seconds.



**Figure 4.** Isochrons for transducer at (0, 2.0 mm) for time=166.65 -seconds with a 10% speed of sound variation

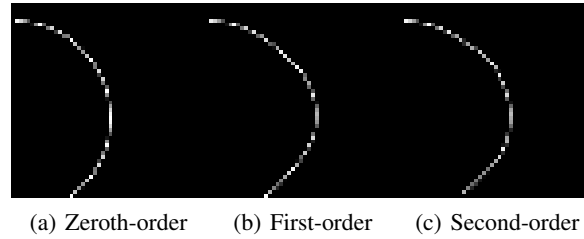


**Figure 5.** Isochrons for transducer at (0, 2.0 mm) for time=166.65 nano-seconds with a 15% speed of sound variation

From these figures, it can be concluded that a speed of variation of 10% or more leads to some differences between the isochrons incorporating second-order and first-order travel time effects.

### 3.2. Iteratively reconstructed images

Figures 6 and 7 show the iteratively reconstructed images incorporating up to third-, second-, first- and zeroth-order travel time effects. For a 5% speed of sound variation, the images reconstructed using third- and second-order corrections are pretty close to the true phantom. The first-order correction offers a better image than the zeroth-order correction, however, it is not as good as the images reconstructed using higher-order corrections. For a 10% speed of sound variation, the image reconstructed using third-order correction is much closer to the true phantom than those reconstructed using the lower-order corrections.

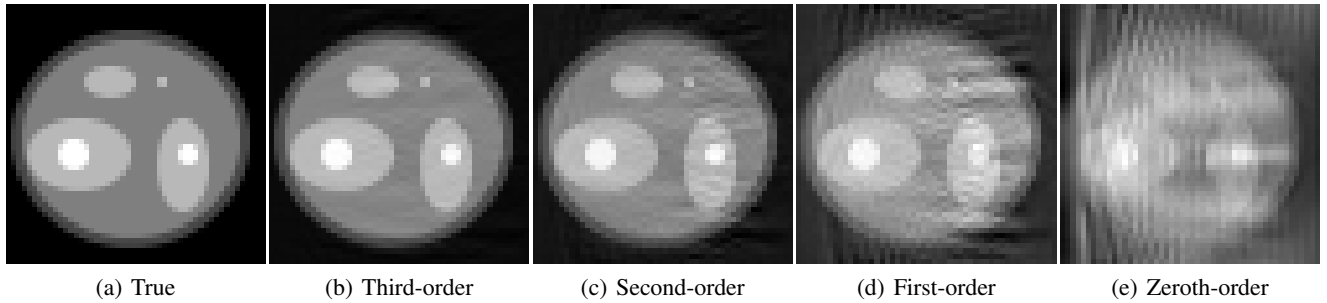


**Figure 6.** Iteratively reconstructed images using fourth-order travel time correction in the forward model with a 5% speed of sound variation, Image were reconstructed using various-order travel time corrections

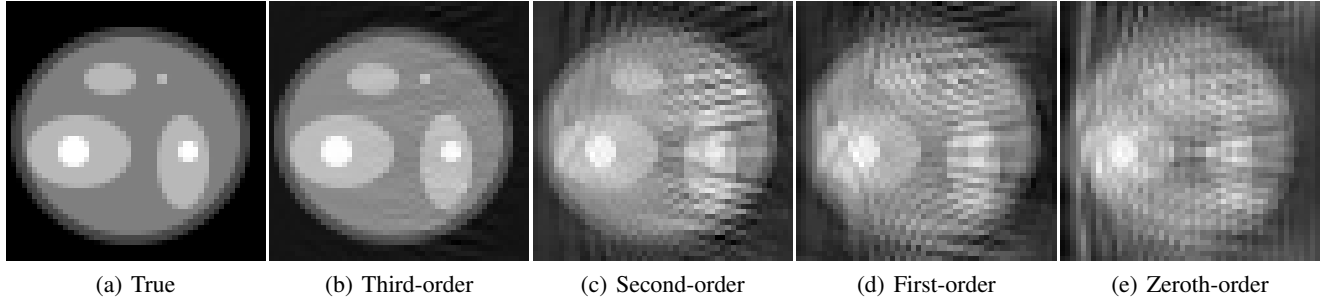


**Figure 7.** Iteratively reconstructed images using fourth-order travel time correction in the forward model with a 10% speed of sound variation, Image were reconstructed using various-order travel time corrections

Figure 8 shows a line profile through the phantom at (0, 2.3 mm). One can see that the difference between third-order and second-order is not so much for a 5% speed of sound variation. However, the difference is more significant for a 10% speed of sound variation especially for objects lying behind the inhomogeneity. The third-order correction offers the best match to the true phantom in this case.

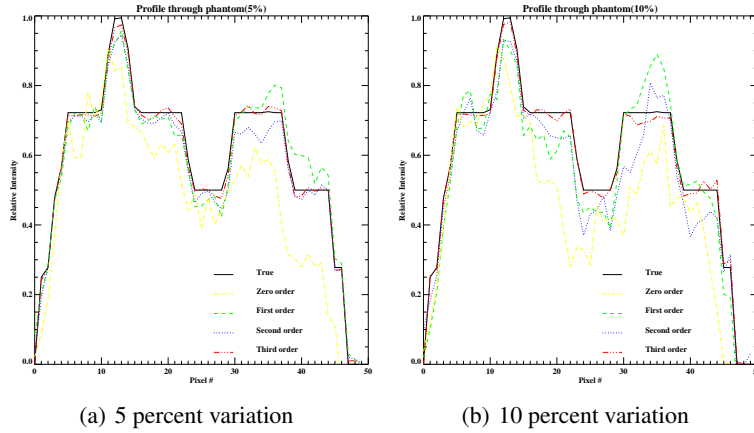


**Figure 8.** Line profile through the phantom at (0,2.3 mm)

## 4. CONCLUSIONS

We derived a higher-order geometrical acoustics approximation to the GRT model in PAT. This incorporates the first-order correction to the pressure amplitude and higher-order correction to the travel times. We found that some differences can be seen in the isochronous curves between second- and first-order corrections when the speed of sound varies by 10% or more. These differences in travel times translated into the reconstructed images as well. Images that were iteratively reconstructed using the third-order travel time corrections were more accurate than those constructed using the lower-order corrections. We will conduct further studies using actual pressure data in an inhomogeneous medium in 3D to quantify the effect of higher-order GA approximation.

## ACKNOWLEDGMENTS

This work was supported in part by a DoD breast cancer pre-doctoral fellowship (W81XWH-08-1-0331) and an American Cancer Society Research Scholar award.



## REFERENCES

1. R. A. Kruger, P. Liu, Y. R. Fang, and C. R. Appledorn, "Photoacoustic ultrasound (PAUS)–reconstruction tomography," *Med Phys* **22**, pp. 1605–1609, Oct 1995.
2. R. S. Cobbold, *Foundations of biomedical ultrasound*, Oxford University Press, New York, 2007.
3. Y. Xu, *Reconstruction in tomography with diffracting sources*, Ph.D. Dissertation, Department of Biomedical Engineering, Texas A and M University, 2003.
4. Y. Xu and L. V. Wang, "Effects of acoustic heterogeneity in breast thermoacoustic tomography," *IEEE Trans. Ultra., Ferro. and Freq. control.* **50**, pp. 1134–1146, Sept 2003.
5. J. Zhang and M. A. Anastasio, "Reconstruction of speed-of-sound and electromagnetic absorption distributions in photoacoustic tomography," *Proc. SPIE* **6086**, pp. 6086 19–1–19–7, 2006.
6. T. G. M. Kolkman, W. Steenbergen, and T. G. van Leeuwen, "Reflection mode photoacoustic measurement of speed of sound," *Optics Express* **15**, pp. 3291–3300, March 2007.
7. S. Manohar, R. G. H. Willemink, , and T. G. van Leeuwen, "Speed-of-sound imaging in a photocaoustic imager," *Proc. of SPIE* **6437**, pp. 64370R–1–64370R–8, 2007.
8. M. Agranovsky and P. Kuchment, "Uniqueness of reconstruction and an inversion procedure for thermoacoustic and photoacoustic tomography with variable speed of sound," *Inverse Problems* **23**, pp. 2089–2012, 2007.
9. Y. Zhen and H. Jiang, "Three-dimensional finite-element-based photoacoustic tomography:Reconstruction algorithm and simulations," *Med. Phys.* **34**, pp. 538–546, Feb. 2007.
10. R. Snieder and D. F. Aldridge, "Perturbation Theory for travel times," *J. Acoust. Soc. Am.* **98**, pp. 1565–1569, Sept 1995.

# Photoacoustic image reconstruction in an attenuating medium using singular-value decomposition

Dimple Modgil\*, Mark A. Anastasio and Patrick J. La Rivière\*

\* Department of Radiology, The University of Chicago  
Department of Biomedical Engineering, Illinois Institute of Technology

## ABSTRACT

Attenuation effects can be significant in photoacoustic tomography (PAT) since the measured pressure signals are broadband and ignoring them may lead to image artifacts and blurring. Previous work by our group had derived a method for modeling the attenuation effect and correcting for it in the image reconstruction. This was done by relating the ideal, unattenuated pressure signals to the attenuated pressure signals via an integral operator. In this work, we explore singular-value decomposition (SVD) of a previously derived 3D integral equation that relates the Fourier transform of the measured pressure with respect to time and two spatial components to the 2D spatial Fourier transform of the optical absorption function. We find that the smallest singular values correspond to wavelet-like eigenvectors in which most of the energy is concentrated at times corresponding to greater depths in tissue. This allows us characterize the ill posedness of recovering absorption information from depth in an attenuating medium. This integral equation can be inverted using standard SVD methods and the optical absorption function can be recovered. We will conduct simulations and derive algorithm for image reconstruction using SVD of this integral operator.

**Keywords:** Optoacoustic tomography, photoacoustic tomography, thermoacoustic tomography, image reconstruction, attenuation, singular-value decomposition

## 1. INTRODUCTION

Optoacoustic/photoacoustic imaging is an emerging imaging technique [1, 2] based on the photoacoustic/optoacoustic effect. This effect refers to acoustic wave generation upon absorption of pulsed optical energy by a medium. The majority of the image reconstruction algorithms in PAT so far have assumed a non-dispersive acoustic medium. The effect of frequency-dependent attenuation on acoustic waves can be significant since PAT uses broadband detection. Reconstructed images may exhibit distortion and artifacts if these effects are not taken into account. Previous work on dispersive acoustic media done by our group [3] focused on incorporating the frequency-dependent attenuation effects into the PAT model. This was done by using a 1D integral operator to relate the ideal pressure to the attenuated pressure. We have also previously derived an inversion formula for the optical absorption function using singular-value decomposition (SVD) [4] based on an approach similar to that of Schotland *et al.* [5] [6], in optical diffusion tomography. This expression directly relates the measured attenuated pressure to the optical absorption function. This formula is applicable in a planar geometry where the array of transducers lies in a plane. In this paper, we will use this approach for image reconstruction in an attenuating medium. We will also conduct noise and resolution studies on the images reconstructed using this approach.

## 2. METHODS

In an attenuating medium, the optoacoustic wave equation includes a loss term [3] and is given by:

$$\nabla^2 p(\mathbf{r}, t) - \frac{\partial^2 p(\mathbf{r}, t)}{c_0^2 \partial t^2} + L(t) * p(\mathbf{r}, t) = -\frac{\beta}{C_p} \frac{\partial}{\partial t} H(\mathbf{r}, t), \quad (1)$$

where  $L(t) = \frac{1}{2\pi} \int d\omega \left\{ k(\omega)^2 - \frac{\omega^2}{c_0^2} \right\} e^{-i\omega t}$ , and

$$k(\omega) = \frac{\omega}{c(\omega)} + i\alpha(\omega), \quad (2)$$

---

Send correspondence to: Dimple Modgil, email: dimple@uchicago.edu

where  $\omega$  is the temporal frequency and  $k(\omega)$  is the complex wave number [7].

For tissues, the ultrasonic attenuation  $\alpha$  is given to a good approximation by:

$$\alpha(\omega) = \alpha_0 |\omega|, \quad (3)$$

where  $\alpha_0 = \frac{10^{-7}}{2\pi} \text{ cm}^{-1} \text{ rad}^{-1} \text{ s}$ .

Using Kramers-Kronig relations, one obtains the dependence of phase velocity  $c(\omega)$  on frequency due to frequency-dependent attenuation as:

$$\frac{1}{c(\omega)} = \frac{1}{c_0} - \frac{2}{\pi} \alpha_0 \ln \left| \frac{\omega}{\omega_0} \right|, \quad (4)$$

where  $\omega_0$  is the reference frequency at which  $c(\omega) = c_0$ .

So for an attenuating medium, on taking the temporal Fourier transform of Eqn. (1) we get:

$$\nabla^2 \tilde{p}(\mathbf{r}, \omega) + k^2(\omega) \tilde{p}(\mathbf{r}, \omega) = -\frac{i\omega\beta}{C_p} A(\mathbf{r}) \tilde{I}(\omega). \quad (5)$$

This equation can be solved using standard Green's function methods as [8]:

$$\tilde{p}(\mathbf{r}, \omega) = -i\eta\omega \tilde{I}(\omega) \int \int \int d^3r' A(\mathbf{r}') G(\mathbf{r} - \mathbf{r}'), \quad (6)$$

where  $\eta \equiv \frac{\beta}{C_p}$  and  $G(\mathbf{r} - \mathbf{r}') = \frac{\exp(ik(\omega)|\mathbf{r} - \mathbf{r}'|)}{4\pi|\mathbf{r} - \mathbf{r}'|}$ .

## 2.1. SVD of integral operator relating attenuated pressure to optical absorption function

Using the angular spectrum expansion of Green's function [9] and by simplifying and discretizing Eqn. (6), one can obtain an integral equation [4]:

$$P_n(\mathbf{q}) = \int dz \tilde{A}(\mathbf{q}, z) K_n(\mathbf{q}, z). \quad (7)$$

This equation can be inverted as [6]:

$$\tilde{A}(\mathbf{q}, z) = \sum_{m,n} K_m^*(\mathbf{q}, z) M_{mn}^{-1}(\mathbf{q}) P_n(\mathbf{q}), \quad (8)$$

where

$$K_n(\mathbf{q}, z) \equiv \frac{-i\eta\omega_n \tilde{I}(\omega_n)}{8\pi^2 \sqrt{q^2 - k_n^2}} \exp\left(-z\sqrt{q^2 - k_n^2}\right), \quad (9)$$

and

$$M_{mn}(\mathbf{q}) \equiv \int dz K_m(\mathbf{q}, z) K_n^*(\mathbf{q}, z). \quad (10)$$

The two-dimensional spatial wave vector  $\mathbf{q}$  is defined as:

$$\mathbf{q} \equiv (k_x, k_y, 0), \quad (11)$$

and the temporal frequency  $\omega$  is discretized as  $\omega_n$ ,  $P_n(\mathbf{q}) \equiv \tilde{p}(\mathbf{q}, \omega_n)$  and  $k_n \equiv k(\omega_n)$ .

The computation of the inverse of this matrix  $M$  is the key step in the procedure to recover the optical absorption function. Its pseudoinverse can be computed by performing an SVD of matrix  $K$ . Some of the eigenvalues of this matrix may be zero or very small. This problem can be avoided by using regularization.

Thus, the procedure for recovering  $A(\mathbf{r})$  is:

1. Take the Fourier transform of the measured pressure (at  $z = 0$ ) with respect to time and the 2D spatial components to obtain  $\tilde{p}(k_x, k_y, \omega)$ .
2. Discretize  $\tilde{p}(k_x, k_y, \omega)$  as  $\tilde{p}(\mathbf{q}, \omega_n)$ .
3. Compute the matrix  $K_n(\mathbf{q}, z)$  using Eqn. (9) .
4. Compute the pseudoinverse of matrix  $M_{mn}(\mathbf{q})$  by performing SVD of matrix  $K$ .
5. Compute  $\tilde{A}(\mathbf{q}, z)$  using Eqn. (8).
6. Take the 2D inverse Fourier transform of  $\tilde{A}(\mathbf{q}, z)$  to obtain  $A(\mathbf{r})$ .

We previously [4] looked at the properties of the matrix  $K$  and its singular values for a medium with non-zero attenuation. We found that  $A(\mathbf{q}, z)$  was much more reliably recovered for  $\mathbf{q}$  with magnitude smaller than the wave number  $\frac{\omega}{c}$  than for larger  $\mathbf{q}$  . We also observed that smaller eigenvalues typically corresponded to eigenvectors with most of their energy at greater depths. The behavior of eigenvectors and eigenvalues indicated that shallower objects can be recovered much better than deeper objects because they correspond to eigenvectors with much higher eigenvalues.

## 2.2. 3D Simulated pressure data

We simulated the 3D attenuated pressure data in planar geometry using two methods. The SVD-based method directly computes the attenuated pressure signals. The Fourier-based method first calculates the ideal pressure and then computes the attenuated pressure from it. We used these two methods to make sure that the results were consistent.

### 2.2.1. SVD-based simulated pressure

We used Eqn. (7) to calculate the attenuated pressure. This was implemented as follows:

1. Take the 2D spatial Fourier transform of the optical absorption function in the  $x$  and  $y$  directions to obtain  $\tilde{A}(\mathbf{q}, z)$ .
2. Construct the matrix  $K_n(\mathbf{q}, z)$  as a function of discrete  $\omega, q$  and  $z$  based on Eqn. (9).
3. Multiply  $\tilde{A}(\mathbf{q}, z)$  by  $K_n(\mathbf{q}, z)$  and sum over  $z$  to obtain  $P_n(\mathbf{q})$ .
4. Take the inverse Fourier transform of  $P_n(\mathbf{q})$  to obtain attenuated pressure  $p(\mathbf{r}, t)$ .

### 2.2.2. Fourier-based simulated pressure

We used the Fourier-based expression described by Kostli *et al.* [10] to calculate the 3D ideal pressure. This expression relates the 3D Fourier transform of the optical absorption function to the pressure as:

$$p(\mathbf{r}, t) = \frac{1}{(2\pi)^3} \int d^3k A(\mathbf{k}) \cos(\omega t) \exp(i\mathbf{k} \cdot \mathbf{r}), \quad (12)$$

where,  $\omega = c_0 \sqrt{k_x^2 + k_y^2 + k_z^2}$ . We evaluated the ideal pressure on the plane  $z = 0$ . We then used the integral expression derived by La Rivière *et al.* [3] to compute the attenuated pressure from the ideal pressure data. Their expression is given by:

$$p(\mathbf{r}, \omega) = \tilde{I}(\omega) \left( \frac{c_0}{c(\omega)} + i\alpha_0 c_0 \operatorname{sgn}(\omega) \right) \int p_{ideal}(\mathbf{r}, t) \exp \left\{ i \left[ \omega \frac{c_0}{c(\omega)} + i\alpha_0 c_0 |\omega| t \right] \right\} dt.^{-1} \quad (13)$$

### 2.3. Image Reconstruction Details

The images were reconstructed using the SVD-based expression using the two different simulated pressures. This was done by performing the SVD of matrix  $K$  to obtain the regularized pseudoinverse of matrix  $M$ . The matrix  $K$  was zero-padded in the temporal frequency domain. The mean value of the eigenvalues of  $M$  for a specific  $q$  was used to regularize the pseudoinverse of  $M$  for that  $q$ . The images were reconstructed on a  $128 \times 128 \times 32$  grid. The number of transducer positions in the  $X - Y$  plane were  $128 \times 128$  and 32 temporal samples were used. The pixel size in the  $X - Y$  plane was set to 0.75 mm. The  $z$ -slice thickness was 0.75 mm. The maximum temporal frequency was set to 1.0 MHz. The temporal sampling interval was set to 500 nsec. The attenuation coefficient was set to  $\alpha_0 = \frac{10^{-7}}{2\pi} \text{ cm}^{-1} \text{ rad}^{-1} \text{ s}$ . The speed of sound  $c_0$  was set to 1500 m/s at  $\frac{\omega_0}{2\pi} = 1 \text{ MHz}$ . A point source was placed at different depths and its image was reconstructed to obtain depth resolution.

## 3. RESULTS

### 3.1. Noiseless Data

The reconstructed images using SVD-based reconstruction are shown below in figure 1. The reconstructed images bear a close resemblance to the actual phantom. There are some spurious artifacts in the reconstructed images due to inter-planar interference and the inexact nature of reconstruction due to regularization of the pseudoinverse of matrix  $M$ .

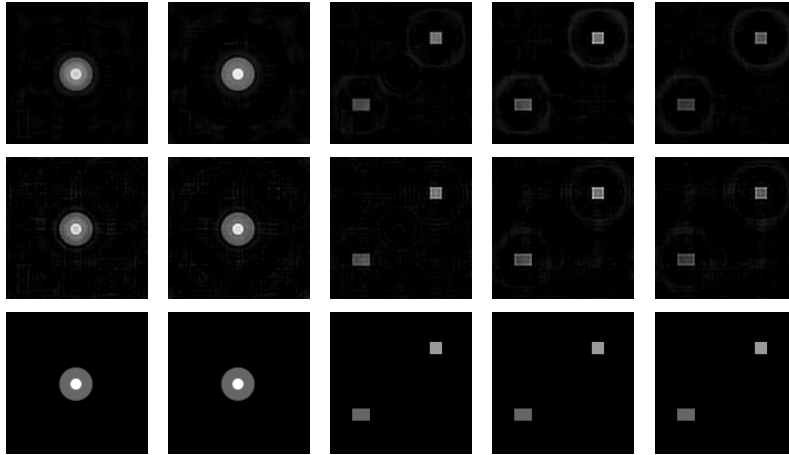


**Figure 1.** Reconstructed  $z$ -slices (0.15 cm, 0.225 cm, 0.3 cm and 0.45 cm) of a 3D phantom using SVD-based image reconstruction approach top: Fourier-based attenuated pressure, middle: SVD-based attenuated pressure, bottom: actual phantom

### 3.2. Noisy Data

Gaussian noise with zero mean with 10% amplitude was added to the pressure data to obtain noisy data. The following images were reconstructed using a bigger transducer size of  $200 \times 200$  and a maximum frequency of 10 MHz since we wanted to evaluate the performance of the SVD-based algorithm at greater depths. Figure 2 shows the reconstructed phantom using noiseless and noisy attenuated pressure.

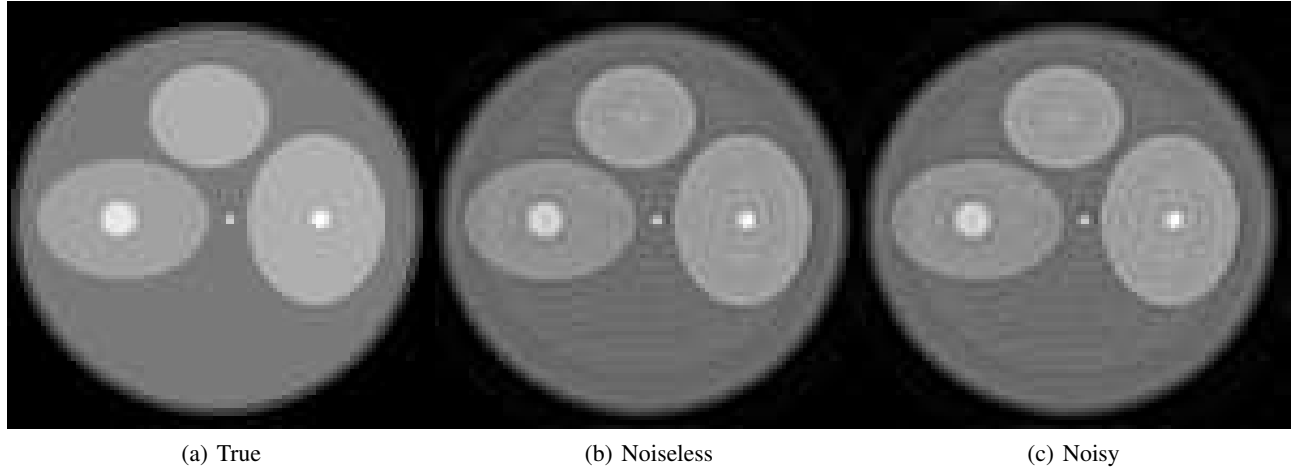


**Figure 2.** Select reconstructed z-plane at a depth of 1.6875 cm reconstructed using noiseless and noisy SVD-based attenuated pressure

Figure 3 shows profiles corresponding to the line  $y = 1.8375$  cm in the slice  $z = 1.6875$  cm of the reconstructed  $A(\mathbf{r})$ .

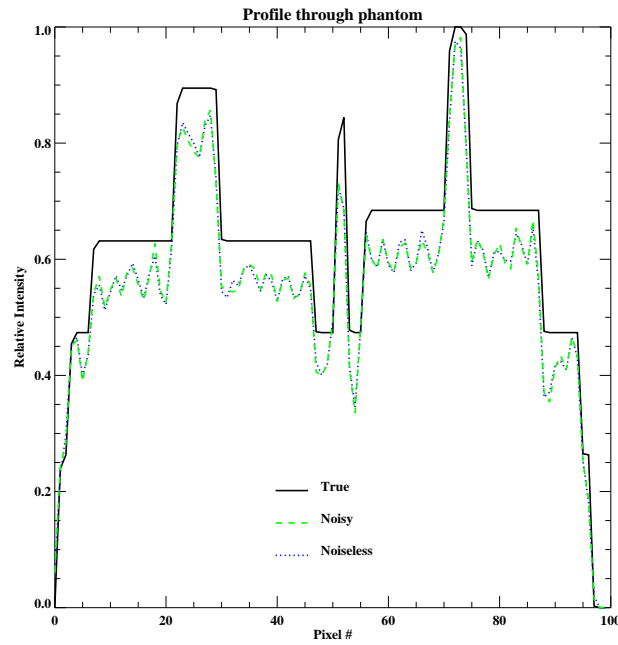


**Figure 3.** Line profile through phantom at depth  $z = 1.6875$  cm and  $y = 1.8375$  cm for noiseless and noisy data

The reconstructed images based on the noisy and noiseless simulated pressures obtained via SVD-based method are in good agreement with the true phantom. The SVD-based image reconstruction algorithm offers comparable images even with noisy data at greater depths.

### 3.3. Depth Resolution

Figure 4 shows the profile through a point source placed at various depths reconstructed using SVD-based attenuated pressure. The SVD-based image reconstruction algorithm shows very good depth resolution.

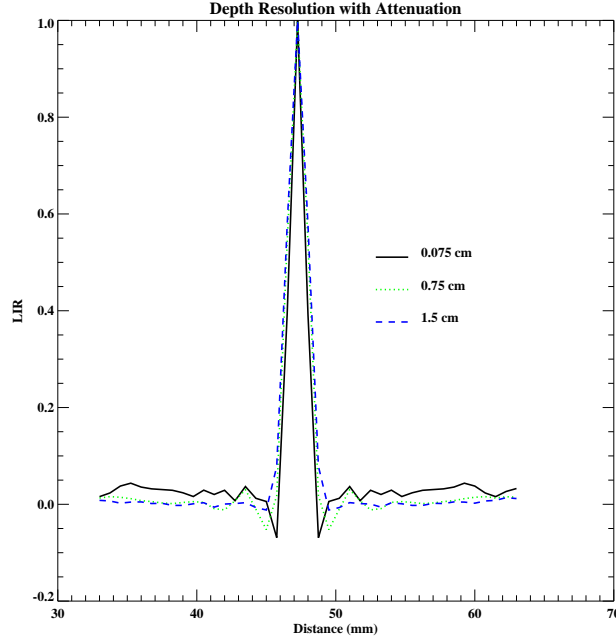


**Figure 4.** Line profile of a point source placed at various depths

#### 4. CONCLUSIONS

We were able to use a previously derived operator relating the attenuated pressure to optical absorption function to reconstruct images in PAT in an attenuating medium for planar geometry. The image reconstruction algorithm based on the SVD of this operator shows very good depth resolution and noise stability. Further studies will include using this algorithm on actual attenuated pressure data.

#### ACKNOWLEDGMENTS

This work was supported in part by a DoD breast cancer pre-doctoral fellowship (W81XWH-08-1-0331) and an American Cancer Society Research Scholar award.

#### REFERENCES

1. R. A. Kruger, D. R. Reinecke, and G. A. Kruger, "Thermoacoustic computed tomography—technical considerations," *Med Phys* **26**, pp. 1832–1837, Sep 1999.
2. M. Xu and L. V. Wang, "Photoacoustic imaging in biomedicine," *Rev. Sci. Instr.* **77**, pp. 041101–1–041101–22, Apr 2006.
3. P. J. La Rivière, J. Zhang, and M. A. Anastasio, "Image reconstruction in optoacoustic tomography for dispersive acoustic media," *Optics Letters* **31**(6), pp. 781–783, 2006.
4. D. Modgil and P. J. La Rivière, "Photoacoustic image reconstruction in an attenuating medium using singular-value decomposition," *NSS-MIC conference proceedings*, 2008.
5. V. A. Markel and J. C. Schotland, "Inverse problem in optical diffusion tomography. I. Fourier-Laplace inversion formulas," *J. Opt. Soc. Am.* **18**, pp. 1336–1347, 2001.
6. V. A. Markel, V. Mital, and J. C. Schotland, "Inverse problem in optical diffusion tomography. III Inversion formulas and singular-value decomposition," *J. Opt. Soc. Am A* **20**, pp. 890–902, May 2003.
7. N. V. Sushilov and R. S. C. Cobbold, "Frequency-domain wave equation and its time-domain solutions in attenuating media," *J. Acoust. Soc. Am.* **115**, pp. 1431–1436, Apr 2004.
8. Y. Xu, D. Feng, and L. V. Wang, "Exact frequency-domain reconstruction for thermoacoustic tomography—I: Planar geometry," *IEEE Trans Med Imaging* **21**, pp. 823–828, Jul 2002.

9. C. L. Matson, "A Diffraction tomographic model of the forward problem using diffuse photon density waves," *Optics Express* **1**, pp. 6–11, Jul 1997.
10. K. P. Kostli, M. Frenz, H. Bebie, and H. P. Weber, "Temporal backward projection of optoacoustic pressure transients using fourier transform methods," *Phys Med Biol* **46**, pp. 1863–1872, Jul 2001.



# Photoacoustic image reconstruction in an attenuating medium using singular-value decomposition

Dimple Modgil and Patrick J. La Rivière

## I. INTRODUCTION

Photoacoustic tomography (PAT) or optoacoustic tomography reconstructs an image of the optical absorption function of a medium using the ultrasound signals induced when it is exposed to pulsed electromagnetic radiation. These signals are generated due to the thermal expansion caused by localized heating from the absorption of pulsed electromagnetic radiation [1]. The majority of the image reconstruction algorithms in PAT so far have assumed a non-dispersive acoustic medium. The effect of frequency-dependent attenuation on acoustic waves can be significant since PAT uses broadband detection. Reconstructed images may exhibit distortion and artifacts if these effects are not taken into account. Previous work on dispersive acoustic media done by our group [2] focused on incorporating the frequency-dependent attenuation effects into the PAT model. In this paper, we will use an approach similar to that by Schotland *et al.* [3] [4], in optical diffusion tomography, to derive an inversion formula for the optical absorption function using singular-value decomposition (SVD). This formula is applicable in a planar geometry where the array of transducers lies in a plane. It provides an insight into the conditioning of the inverse problem and offers a promising method for image reconstruction in an attenuating medium.

## II. METHODS

Under the constraints of negligible thermal diffusion, the photoacoustic pressure,  $p(\mathbf{r}, t)$  satisfies the wave equation [5] [6]:

$$\nabla^2 p(\mathbf{r}, t) - \frac{1}{c_0^2} \frac{\partial^2}{\partial t^2} p(\mathbf{r}, t) = -\frac{\beta}{C_p} \frac{\partial}{\partial t} H(\mathbf{r}, t), \quad (1)$$

where  $c_0$  is the speed of sound in the medium,  $C_p$  is the specific heat, and  $\beta$  is the coefficient of thermal expansion.  $H(\mathbf{r}, t)$  is the heating function that denotes the energy deposited per unit time per unit volume in the medium by the illuminating optical pulse. One can express  $H(\mathbf{r}, t)$  as:

$$H(\mathbf{r}, t) = A(\mathbf{r})I(t),$$

where  $A(\mathbf{r})$  is the optical energy absorption at  $\mathbf{r}$  and  $I(t)$  is the temporal profile of the optical pulse. On taking the Fourier transform of the wave equation with respect to time, one obtains:

$$\nabla^2 \tilde{p}(\mathbf{r}, \omega) + \frac{\omega^2}{c_0^2} \tilde{p}(\mathbf{r}, \omega) = \frac{i\omega\beta}{C_p} A(\mathbf{r})\tilde{I}(\omega), \quad (2)$$

where  $\omega$  is the temporal frequency.

In the presence of attenuation, the wave number becomes complex and is given by [7]:

$$k(\omega) = \frac{\omega}{c(\omega)} + i\alpha(\omega). \quad (3)$$

For tissues, the ultrasonic attenuation  $\alpha$  is given to a good approximation by:

$$\alpha(\omega) = \alpha_0 |\omega|. \quad (4)$$

Using Kramers-Kronig relations, one obtains the dependence of phase velocity  $c(\omega)$  on frequency due to frequency-dependent attenuation as:

$$\frac{1}{c(\omega)} = \frac{1}{c_0} - \frac{2}{\pi} \alpha_0 \ln \left| \frac{\omega}{\omega_0} \right|. \quad (5)$$

So for an attenuating medium, eqn. (2) becomes:

$$\nabla^2 \tilde{p}(\mathbf{r}, \omega) + k^2(\omega) \tilde{p}(\mathbf{r}, \omega) = -\frac{i\omega\beta}{C_p} A(\mathbf{r})\tilde{I}(\omega). \quad (6)$$

This equation can be solved using standard Green's function methods as [6]:

$$\tilde{p}(\mathbf{r}, \omega) = -i\eta\omega\tilde{I}(\omega) \int \int \int d^3r' A(\mathbf{r}') G(\mathbf{r} - \mathbf{r}'), \quad (7)$$

where  $\eta = \frac{\beta}{C_p}$ .

### A. Angular spectrum expansion of the measured pressure signals

The angular spectrum expansion of the Green's function is given by [8]:

$$G(r) = \frac{\exp(iKr)}{4\pi r} = \frac{1}{8\pi^2} \int \int \frac{1}{\sqrt{\alpha_x^2 + \alpha_y^2 - k^2}} \times \exp\left(-|z|\sqrt{\alpha_x^2 + \alpha_y^2 - k^2} + ix\alpha_x + iy\alpha_y\right) d\alpha_x d\alpha_y. \quad (8)$$

Substitute this in eqn. (7) and consider the pressure measurements on the plane  $z = 0$  and we get:

$$\begin{aligned}\tilde{p}(x, y, 0, \omega) &= \frac{-i\eta\omega\tilde{I}(\omega)}{8\pi^2} \int \int d^3r' A(x', y', z') \\ &\times \int \int d\alpha_x d\alpha_y \frac{1}{\sqrt{\alpha_x^2 + \alpha_y^2 - k^2}} \\ &\times \exp\left(-|z'|\sqrt{\alpha_x^2 + \alpha_y^2 - k^2} + ix'\alpha_x + iy'\alpha_y\right).\end{aligned}\quad (9)$$

We assume that the photoacoustic object lies in the plane  $z' \geq 0$ . On taking the Fourier transform on both sides and reducing the resulting expression one obtains the angular spectrum expansion of measured photoacoustic pressure as:

$$\begin{aligned}\tilde{p}(k_x, k_y, \omega) &= \frac{-i\eta\omega\tilde{I}(\omega)}{8\pi^2\sqrt{k_x^2 + k_y^2 - k^2(\omega)}} \int dz' \tilde{A}(k_x, k_y, z') \\ &\times \exp\left(-z'\sqrt{k_x^2 + k_y^2 - k^2(\omega)}\right).\end{aligned}\quad (10)$$

1) *SVD of integral operator relating pressure to optical absorption coefficient*: We follow Schotland's [3] [4] approach to optical diffusion tomography to obtain an integral operator relating the measured attenuated pressure to the optical absorption coefficient.

Define two-dimensional spatial wave vector  $\mathbf{q}$  as:

$$\mathbf{q} \equiv (k_x, k_y, 0). \quad (11)$$

Discretize the temporal frequency,  $\omega$  as  $\omega_n$ . One can then write the pressure as:

$$\begin{aligned}\tilde{p}(\mathbf{q}, \omega_n) &= \frac{-i\eta\omega_n\tilde{I}(\omega_n)}{8\pi^2\sqrt{q^2 - k^2(\omega_n)}} \int dz \tilde{A}(\mathbf{q}, z) \\ &\times \exp\left(-z\sqrt{q^2 - k^2(\omega_n)}\right).\end{aligned}\quad (12)$$

Define  $P_n(\mathbf{q}) \equiv \tilde{p}(\mathbf{q}, \omega_n)$ ,  $k_n \equiv k(\omega_n)$  and

$$K_n(\mathbf{q}, z) \equiv \frac{-i\eta\omega_n\tilde{I}(\omega_n)}{8\pi^2\sqrt{q^2 - k_n^2}} \exp\left(-z\sqrt{q^2 - k_n^2}\right). \quad (13)$$

Thus, equation (12) becomes:

$$P_n(\mathbf{q}) = \int dz \tilde{A}(\mathbf{q}, z) K_n(\mathbf{q}, z). \quad (14)$$

This equation can be inverted as [4]:

$$\tilde{A}(\mathbf{q}, z) = \sum_{m,n} K_m^*(\mathbf{q}, z) M_{mn}^{-1}(\mathbf{q}) P_n(\mathbf{q}), \quad (15)$$

where

$$M_{mn}(\mathbf{q}) = \int dz K_m(\mathbf{q}, z) K_n^*(\mathbf{q}, z). \quad (16)$$

Taking the inverse Fourier transform of eqn. (15) with respect to  $\mathbf{q}$  gives:

$$A(\mathbf{r}) = \frac{1}{(2\pi)^2} \int d^2q \exp(i\mathbf{q}\cdot\boldsymbol{\rho}) \sum_{m,n} K_m^*(\mathbf{q}, z) M_{mn}^{-1}(\mathbf{q}) P_n(\mathbf{q}). \quad (17)$$

Define  $Q_n(\mathbf{q}) \equiv \sqrt{q^2 - k_n^2}$ . This function  $Q_n(\mathbf{q})$  is complex for non-zero attenuation. One can simplify equation (16) to obtain:

$$\begin{aligned}M_{mn}(\mathbf{q}) &= \int_0^\infty dz \frac{\eta^2\omega_m\omega_n I(\omega_m)I(\omega_n)}{(8\pi^2)^2 Q_m(\mathbf{q})Q_n^*(\mathbf{q})} \\ &\times \exp(-z(Q_m(\mathbf{q}) + Q_n^*(\mathbf{q})))\end{aligned}\quad (18)$$

This can be reduced to:

$$M_{mn}(\mathbf{q}) = \frac{\eta^2\omega_m\omega_n I(\omega_m)I(\omega_n)}{(8\pi^2)^2 Q_m(\mathbf{q})Q_n^*(\mathbf{q})} \left( \frac{1}{(Q_m(\mathbf{q}) + Q_n^*(\mathbf{q}))} \right). \quad (19)$$

The computation of the inverse of this matrix is the key step in the procedure to recover the optical absorption function. Its pseudoinverse can be computed by performing SVD of matrix  $K$ . Some of the eigenvalues of this matrix may be zero or very small. One will need to use regularization to circumvent this problem.

Thus, the procedure for recovering  $A(\mathbf{r})$  is:

- 1) Take the Fourier transform of the measured pressure (at  $z = 0$ ) with respect to time and the 2D spatial components to obtain  $\tilde{p}(k_x, k_y, \omega)$ .
- 2) Discretize  $\tilde{p}(k_x, k_y, \omega)$  as  $\tilde{p}(\mathbf{q}, \omega_n)$ .
- 3) Compute the matrix  $K_n(\mathbf{q}, z)$  using eqn. (13).
- 4) Compute the pseudoinverse of matrix  $M_{mn}(\mathbf{q})$  by performing SVD of matrix  $K$ .
- 5) Compute  $\tilde{A}(\mathbf{q}, z)$  using eqn. (15).
- 6) Take the 2D inverse Fourier transform of  $\tilde{A}(\mathbf{q}, z)$  to obtain  $A(\mathbf{r})$ .

2) *Calculation of eigenvalues of  $M$  matrix with non-zero attenuation*: We looked at the properties of the matrix  $K$  and its singular values for a medium with non-zero attenuation. We computed this matrix for a tissue with attenuation  $\alpha_0 = \frac{10^{-7}}{2\pi} \text{cm}^{-1} \text{rad}^{-1} \text{s}$ . A set of 32 discrete temporal frequencies and 64 discrete spatial frequencies was used. Temporal frequencies ranged from 0 to 12.17 MHz. and spatial frequencies ranged from 0 to 82.23  $\text{cm}^{-1}$ . We performed an SVD of the matrix  $K$ . The eigenvalues of the matrix  $M$  were obtained from the singular values of matrix  $K$ .

The surface plot of eigenvalues of  $M$  vs. the spatial frequency  $q$  is shown in figure 1. From this plot, one can see that values of 2D spatial frequency vector  $\mathbf{q}$  that are much smaller than the wave vector are recovered much better than the ones that are of higher magnitude. Figure 2 shows the variation of eigenvectors of  $K^+K$  with  $z$ . In this figure, the vertical direction is increasing depth and the horizontal direction is decreasing eigenvalues. Figure 3 shows the variation of the eigenvectors of matrix  $K^+K$  with depth for a specific eigenvalue. In these plots, a lower column number corresponds to a higher eigenvalue. From these plots one concludes that:

- 1) The values of 2D spatial frequency wave vector ' $\mathbf{q}$ ' that are smaller than the wave vector are recovered much better.
- 2) The eigenvectors that are non-zero at greater depths correspond to smaller eigenvalues.

The behavior of eigenvectors and eigenvalues indicates that shallower objects can be recovered much better than deeper objects because they correspond to eigenvectors with much higher eigenvalues.

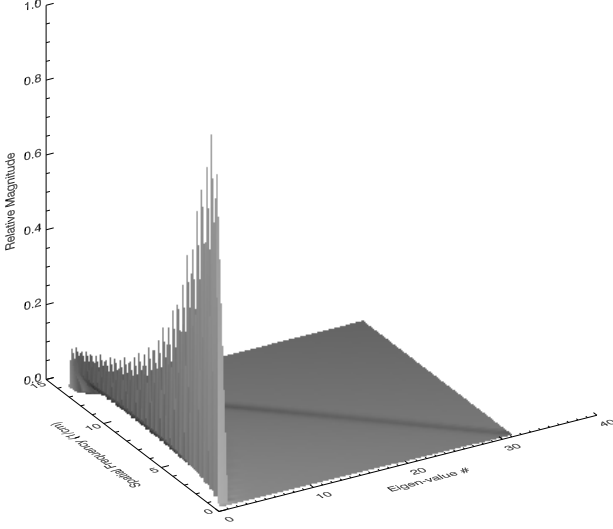


Figure 1. Plot of eigenvalues of  $M$  vs.  $q$

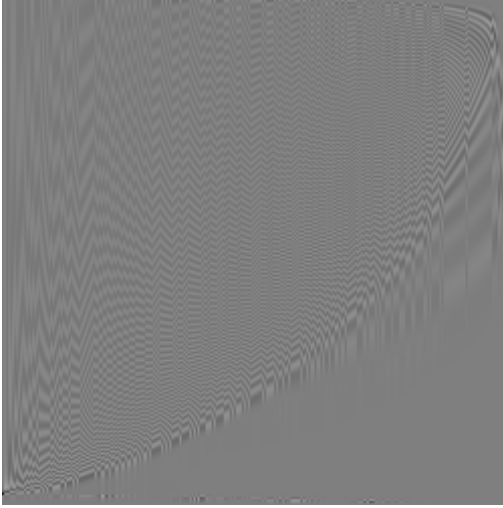
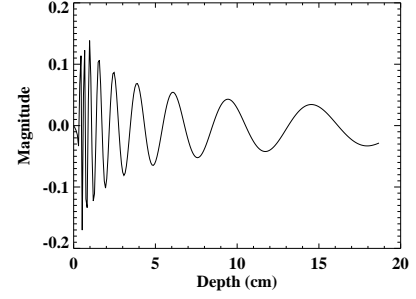


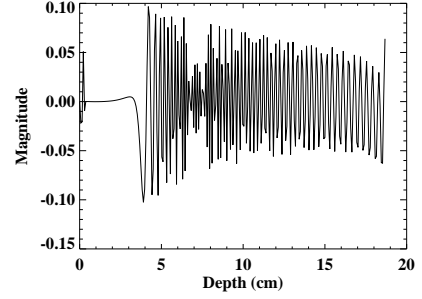
Figure 2. Real-part of a set of eigenvectors of matrix  $K^+K$  for a specific  $q$ ,  $x$ -axis: decreasing eigenvalues,  $y$ -axis: increasing depth

### B. 3D Simulated pressure data

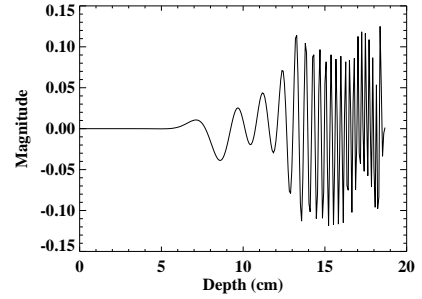
We simulated the 3D attenuated pressure data in planar geometry using two methods. The SVD-based method directly computes the attenuated pressure signals. The Fourier-based method first calculates the ideal pressure and then computes



(a) Column=10



(b) Column=125



(c) Column=230

Figure 3. Variation of select eigenvectors with depth

the attenuated pressure from it. We used these two methods to make sure that the results were consistent and to avoid the possibility of an inverse crime.

1) *SVD-based simulated pressure:* We used eqn. (14) to calculate the attenuated pressure. This was implemented as follows:

- 1) Take the 2D spatial Fourier transform of the optical absorption function in the  $x$  and  $y$  directions to obtain  $\tilde{A}(\mathbf{q}, z)$ .
- 2) Construct the matrix  $K_n(\mathbf{q}, z)$  as a function of discrete  $\omega, q$  and  $z$  based on eqn. (13).
- 3) Multiply  $\tilde{A}(\mathbf{q}, z)$  by  $K_n(\mathbf{q}, z)$  and sum over  $z$  to obtain  $P_n(\mathbf{q})$ .
- 4) Take the inverse Fourier transform of  $P_n(\mathbf{q})$  to obtain attenuated pressure  $p(\mathbf{r}, t)$ .

2) *Fourier-based simulated pressure:* We used the Fourier-based expression described by Kostli *et al.* [9] to calculate the 3D ideal pressure. This expression relates the 3D Fourier transform of the optical absorption function to the pressure as:

$$p(\mathbf{r}, t) = \frac{1}{(2\pi)^3} \int d^3k A(\mathbf{k}) \cos(\omega t) \exp(i\mathbf{k} \cdot \mathbf{r}), \quad (20)$$

where,  $\omega = c_0 \sqrt{k_x^2 + k_y^2 + k_z^2}$ . We evaluated the ideal pressure on the plane  $z = 0$ . We then used the integral expression derived by La Rivière *et al.* [2] to compute the attenuated pressure from the ideal pressure data. Their expression is given by:

$$p(\mathbf{r}, \omega) = \tilde{I}(\omega) \left( \frac{c_0}{c(\omega)} + i\alpha_0 c_0 \text{sgn}(\omega) \right)^{-1} \times \int p_{ideal}(\mathbf{r}, t) \exp \left\{ i \left[ \omega \frac{c_0}{c(\omega)} + i\alpha_0 c_0 |\omega| t \right] \right\} dt. \quad (21)$$

### C. Image Reconstruction Details

The images were reconstructed using the SVD-based expression using the two different simulated pressures. This was done by performing the SVD of matrix  $K$  to obtain the regularized pseudoinverse of matrix  $M$ . The mean value of the eigenvalues of  $M$  for a specific  $q$  was used to regularize the pseudoinverse of  $M$  for that  $q$ . The images were reconstructed on a  $128 \times 128 \times 32$  grid. The number of transducer positions in the  $X - Y$  plane were  $128 \times 128$  and 32 temporal samples were used. The pixel size in the  $X - Y$  plane was set to 0.75 mm. The  $z$ -slice thickness was 0.75 mm. The maximum temporal frequency was set to 1.0 MHz. The temporal sampling interval was set to 500 nsec. The attenuation coefficient was set to  $\alpha_0 = \frac{10^{-7}}{2\pi} \text{ cm}^{-1} \text{ rad}^{-1} \text{ s}$ . The speed of sound  $c_0$  was set to 1500 m/s at  $\frac{\omega_0}{2\pi} = 1 \text{ MHz}$ .

## III. RESULTS

The reconstructed images using SVD-based reconstruction are shown below in figure 4. The reconstructed images bear a close resemblance to the actual phantom. There are some spurious artifacts in the reconstructed images due to interplanar interference and the inexact nature of reconstruction due to regularization of the pseudoinverse of matrix  $M$ .

Figure 5 shows profiles corresponding the line  $y = 4.725 \text{ cm}$  in the slice  $z = 0.225 \text{ cm}$  of the reconstructed  $A(\mathbf{r})$ .

The reconstructed images based on the simulated pressures obtained via SVD-based and Fourier-based methods are in good agreement with the true phantom.

## IV. DISCUSSION

We have derived an SVD-based algorithm to reconstruct the optical absorption function in PAT in an attenuating medium. We looked at the eigenvalues of the matrix  $M$  which is used to recover the optical absorption function. We found that smaller values of 2D spatial frequency vector  $\mathbf{q}$  are recovered much better than the larger values. The SVD approach to

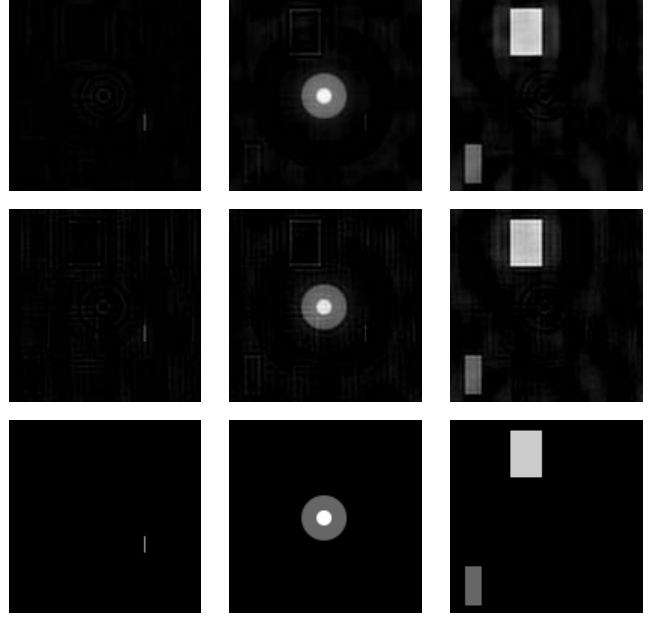


Figure 4. Reconstructed  $z$ -slices (0.15 cm, 0.225 cm and 0.30 cm) of a 3D phantom using SVD-based image reconstruction approach top: Fourier-based attenuated pressure, middle: SVD-based attenuated pressure, bottom: actual phantom

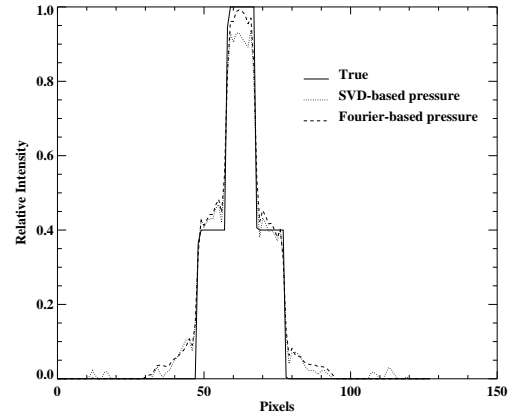


Figure 5. Profile along the line  $y = 4.725 \text{ cm}$ ,  $z = 0.225 \text{ cm}$ , solid line - true profile, dotted line - using SVD-based pressure, dashed line - using Fourier-based pressure

the attenuation problem in PAT offers a promising method for image reconstruction that is direct and computationally efficient. It also provides a way to study the conditioning of this inverse problem. Further studies need to be conducted with actual attenuated pressure data. We also need to perform noise and resolution studies to evaluate the image quality of images reconstructed using the SVD-based image reconstruction method.

## V. ACKNOWLEDGEMENTS

This work was partially supported via a DoD breast cancer pre-doctoral fellowship (W81XWH-08-1-0331) and an American Cancer Society Research Scholar award.

## REFERENCES

- [1] M. Xu and L. V. Wang, "Photoacoustic imaging in biomedicine," *Rev. Sci. Instr.* **77**, pp. 041101–1–041101–22, Apr 2006.
- [2] P. J. La Rivière, J. Zhang, and M. A. Anastasio, "Image reconstruction in optoacoustic tomography for dispersive acoustic media," *Optics Letters* **31**(6), pp. 781–783, 2006.
- [3] V. A. Markel and J. C. Schotland, "Inverse problem in optical diffusion tomography. I. Fourier-Laplace inversion formulas," *J. Opt. Soc. Am.* **18**, pp. 1336–1347, 2001.
- [4] V. A. Markel, V. Mital, and J. C. Schotland, "Inverse problem in optical diffusion tomography. III Inversion formulas and singular-value decomposition," *J. Opt. Soc. Am A* **20**, pp. 890–902, May 2003.
- [5] R. A. Kruger, P. Liu, Y. R. Fang, and C. R. Appledorn, "Photoacoustic ultrasound (PAUS)–reconstruction tomography," *Med Phys* **22**, pp. 1605–1609, Oct 1995.
- [6] Y. Xu, D. Feng, and L. V. Wang, "Exact frequency-domain reconstruction for thermoacoustic tomography–I: Planar geometry," *IEEE Trans Med Imaging* **21**, pp. 823–828, Jul 2002.
- [7] N. V. Sushilov and R. S. C. Cobbold, "Frequency-domain wave equation and its time-domain solutions in attenuating media," *J. Acoust. Soc. Am.* **115**, pp. 1431–1436, Apr 2004.
- [8] C. L. Matson, "A Diffraction tomographic model of the forward problem using diffuse photon density waves," *Optics Express* **1**, pp. 6–11, Jul 1997.
- [9] K. P. Kostli, M. Frenz, H. Bebie, and H. P. Weber, "Temporal backward projection of optoacoustic pressure transients using fourier transform methods," *Phys Med Biol* **46**, pp. 1863–1872, Jul 2001.